

# *Global mean sea level over the past 4.5 million years*

Article

Accepted Version

Clark, P. U., Shakun, J. D., Rosenthal, Y., Pollard, D., Hostetler, S. W., Köhler, P., Bartlein, P. J., Gregory, J. M. ORCID: <https://orcid.org/0000-0003-1296-8644>, Zhu, C., Schrag, D. P., Liu, Z. and Pisias, N. G. (2025) Global mean sea level over the past 4.5 million years. *Science*, 390 (6770). eadv8389. ISSN 1095-9203 doi: 10.1126/science.adv8389 Available at <https://centaur.reading.ac.uk/125301/>

It is advisable to refer to the publisher's version if you intend to cite from the work. See [Guidance on citing](#).

To link to this article DOI: <http://dx.doi.org/10.1126/science.adv8389>

Publisher: American Association for the Advancement of Science

All outputs in CentAUR are protected by Intellectual Property Rights law, including copyright law. Copyright and IPR is retained by the creators or other copyright holders. Terms and conditions for use of this material are defined in the [End User Agreement](#).

[www.reading.ac.uk/centaur](http://www.reading.ac.uk/centaur)

**CentAUR**

Central Archive at the University of Reading  
Reading's research outputs online

## Global sea level over the past 4.5 million years

Peter U. Clark<sup>1,2,†</sup>, Jeremy D. Shakun<sup>3,†</sup>, Yair Rosenthal<sup>4,5</sup>, David Pollard<sup>6</sup>, Steven W. Hostetler<sup>1</sup>, Peter Köhler<sup>7</sup>, Patrick J. Bartlein<sup>8</sup>, Jonathan M. Gregory<sup>9,10</sup>, Chenyu Zhu<sup>11</sup>, Daniel P. Schrag<sup>12</sup>, Zhengyu Liu<sup>13</sup>, Nicklas G. Pisias<sup>1</sup>

<sup>1</sup>College of Earth, Ocean, and Atmospheric Sciences, Oregon State University, Corvallis, OR 97331

<sup>2</sup>School of Geography and Environmental Sciences, University of Ulster, Coleraine, Northern Ireland, UK BT52 1SA

<sup>3</sup>Department of Earth and Environmental Sciences, Boston College, Chestnut Hill, MA 02467

<sup>4</sup>Department of Marine and Coastal Science, Rutgers The State University, New Brunswick, NJ 08901

<sup>5</sup>Department of Earth and Planetary Sciences, Rutgers The State University, New Brunswick, NJ 08901

<sup>6</sup>Earth and Environmental Systems Institute, Pennsylvania State University, University Park, PA 16802

<sup>7</sup>Alfred-Wegener-Institut Helmholtz-Zentrum für Polar- und Meeresforschung, Bremerhaven, Germany

<sup>8</sup>Department of Geography, University of Oregon, Eugene, OR 97403-1251

<sup>9</sup>National Center for Atmospheric Science, University of Reading, Reading, UK  
<sup>10</sup>1.5–5.2° N, 11–25° E, 1–1000 m

<sup>10</sup>Met Office Hadley Centre, Exeter, UK

<sup>11</sup>Institute of Atmospheric Physics, Chinese Academy of Sciences, Beijing, China

<sup>12</sup>Department of Earth and Planetary Sciences, Harvard University, Cambridge, MA 02138

<sup>13</sup>Department of Geography, The Ohio S

\*Correspondence to: [clarkp@onid.oregonstate.edu](mailto:clarkp@onid.oregonstate.edu)

†These authors contributed equally to this work.

31    **Abstract**

32    The history of global mean sea level (GMSL) during the late Cenozoic remains uncertain. Here  
33    we use a new reconstruction of changes in  $\delta^{18}\text{O}$  of seawater to reconstruct GMSL over the past 4.5  
34    million years that accounts for temperature-driven changes in the  $\delta^{18}\text{O}$  of the main ice sheets.  
35    Between 4.5 and 3 million years ago (Ma), sea-level highstands remained up to 20 m above present  
36    while the first lowstands below present suggest onset of Northern Hemisphere (NH) glaciation at  
37    4 Ma. Intensification of NH glaciation occurred from 3 Ma to 2.5 Ma, culminating in lowstands  
38    that were comparable to or lower than the Last Glacial Maximum lowstand 21 ka and that  
39    reoccurred throughout much of the Pleistocene. We attribute the middle Pleistocene transition in  
40    ice-sheet variability to modulation of 41-kyr obliquity forcing by an increase in  $\sim$ 100-kyr CO<sub>2</sub>  
41    variability.

42

43 The record of  $\delta^{18}\text{O}$  measured in benthic foraminifera shells ( $\delta^{18}\text{O}_b$ ) (Fig. 1A) is widely used  
44 to represent the long-term evolution of combined changes in ocean temperature and global mean  
45 sea level (GMSL) over the Cenozoic (1-5) as well as to evaluate the response of the climate system  
46 to forcings on orbital and tectonic timescales ( $10^4$ - $10^6$  yr) (6-9). The fidelity of this record as a  
47 global signal has improved with the stacking of multiple records that increases the signal-to-noise  
48 ratio (10-12) and the use of several independent dating methods that provide a robust chronology  
49 (1, 11, 13, 14). Different strategies have then been used to decompose the  $\delta^{18}\text{O}_b$  record into its  
50 temperature ( $\delta^{18}\text{O}_T$ ) and seawater ( $\delta^{18}\text{O}_{\text{sw}}$ ) components, with the former reflecting the temperature  
51 that the benthic foraminifera shells formed in (larger  $\delta^{18}\text{O}_T$  in lower temperature) and the latter  
52 largely reflecting global ice volume (larger  $\delta^{18}\text{O}_{\text{sw}}$  when more land ice). Although these strategies  
53 share the same goal, their different underlying assumptions have resulted in solutions with  
54 pronounced differences during the late Pliocene, early Pleistocene (beginning 2.6 Ma), and the  
55 middle Pleistocene transition (MPT) (1.5-0.9 Ma) (fig. S1), thus confounding understanding of  
56 these critical periods of late-Cenozoic climate and GMSL change.

57 We address these issues by reconstructing GMSL for the past 4.5 million years (Myr) that  
58 circumvents several shortcomings associated with previous reconstructions (see supporting  
59 information, section 1). Using our new reconstruction of changes in global mean ocean  
60 temperature ( $\Delta\text{MOT}$ ), we previously decomposed a  $\delta^{18}\text{O}_b$  stack (12) that includes a correction for  
61 possible diagenesis (15, 16) and the carbonate-ion effect on foraminifera (17) into its  $\delta^{18}\text{O}_T$  and  
62  $\delta^{18}\text{O}_{\text{sw}}$  components (18). Here we convert our  $\delta^{18}\text{O}_{\text{sw}}$  reconstruction (fig. S2C) to GMSL by  
63 applying a mass-balance approach that conserves  $\delta^{18}\text{O}$  changes of the global ocean and the North  
64 American (Laurentide and Cordilleran) (NAIS), Eurasian (EUR), Greenland (GRN), and Antarctic  
65 (ANT) ice sheets, including loss of marine-based ANT ice (19, 20) (see the supplementary

66 materials, section 2). In doing so, our model accounts for time-varying temperature (21) and ice-  
67 volume effects on the  $\delta^{18}\text{O}$  of ice sheets ( $\delta^{18}\text{O}_i$ ) over the past 4.5 Myr that yields a variable  
68 relationship between  $\delta^{18}\text{O}_{\text{sw}}$  and sea level (fig. S3), as opposed to methods that convert  $\delta^{18}\text{O}_{\text{sw}}$  to  
69 sea level using a constant linear scaling between  $\delta^{18}\text{O}_{\text{sw}}$  and sea level (22-26) or a variable scaling  
70 developed for just the last glacial cycle (27, 28).

71 **Global mean sea level over the past 4.5 Myr**

72 Our new reconstruction (Fig. 1C) shows that GMSL was largely above present from 4.5-  
73 4.0 Ma, with sea-level highstands of ~20 m and sea-level fluctuations of 5-20 m suggesting  
74 contributions likely from some combination of changes in GRN and ANT ice sheets although  
75 contributions from NAIS or EUR ice sheets cannot be excluded. Subsequent highstands between  
76 4 and 3 Ma remained 15-20 m above present but lowstands now began to extend regularly below  
77 present by as much as -50 to -80 m thus marking the onset of extensive NH (NAIS, EUR) glaciation  
78 at ~4 Ma. The intensification of NH glaciation from 3 Ma to 2.5 Ma was marked by highstands  
79 that decreased to near-modern levels and lowstands that progressively decreased from  $-55\pm29$  m  
80 at 3 Ma to  $-151\pm25$  m at 2.52 Ma, which is comparable to or lower than the Last Glacial Maximum  
81 (LGM, 21 ka) lowstand ( $-132\pm15$  m) (Fig. 1C). Since 2.5 Ma, sea-level highstands have been  
82 within +10 m of present except between 2.25 Ma to 1.45 Ma when they remained as much as 50  
83 m below present, suggesting incomplete deglaciation of NH ice sheets, while fluctuations of large  
84 LGM-size ice sheets continued throughout the Pleistocene.

85 Three factors used to derive our GMSL reconstruction combine to indicate that early  
86 Pleistocene ice sheets were comparable in size to the LGM in contrast to several previous  
87 reconstructions that suggest that such large ice sheets did not appear until after the MPT (fig. S6A-  
88 D). First, with a  $\Delta\text{MOT}$  that is ~50% of a corresponding change in global mean sea surface

89 temperature ( $\Delta$ SST) before the MPT (18), the increasing (cooling) trend of  $\delta^{18}\text{O}_T$  is smaller in our  
90 reconstruction than if  $\Delta\text{MOT}:\Delta\text{SST}=1$  is assumed throughout the Pleistocene. Being a residual  
91 from the observed  $\delta^{18}\text{O}_b$ , our  $\delta^{18}\text{O}_{\text{sw}}$  is thus more negative during the Pliocene and has a larger  
92 increasing trend between 3.0-2.5 Ma (compare figs. S2A and S2B). Second, because  $\Delta\text{MOT}:\Delta\text{SST}$   
93 was smaller during the early Pleistocene, so was glacial-interglacial MOT variability (15), limiting  
94 the contribution of  $\delta^{18}\text{O}_T$  to glacial cycles in  $\delta^{18}\text{O}_b$ , in contrast to the middle and late Pleistocene  
95 when ocean temperature and ice volume exerted similar-size controls on  $\delta^{18}\text{O}_b$ . Third, we find that  
96 higher global mean surface temperature (GMST) during the early Pleistocene caused the ice sheets  
97 to be isotopically heavier (fig. S3D). This reduced their influence on  $\delta^{18}\text{O}_{\text{sw}}$  relative to the  
98 isotopically lighter ice sheets during the middle and late Pleistocene. At the same time, given our  
99 reconstructed  $\delta^{18}\text{O}_T$ , Ref. (18) identified the need to remove a spurious increasing trend from the  
100  $\delta^{18}\text{O}_b$  stack attributed to diagenesis (15, 16) or the carbonate-ion effect on benthic foraminifera  
101 (17) that, if unaccounted for, would have resulted in even more positive Pliocene  $\delta^{18}\text{O}_{\text{sw}}$  values  
102 and larger early Pleistocene ice volumes than in our reconstruction (compare figs. S2B and S2C  
103 and figs. S2E and S2F).

104 The spectral characteristics of our GMST reconstruction are dominated by 41-kyr variance  
105 until  $\sim$ 1.2 Ma, followed by the emergence of a  $\sim$ 100-kyr signal during the MPT with similar  
106 concentrations of  $\sim$ 100-kyr and 41-kyr variance and a small concentration of 23-kyr variance over  
107 the past 0.8 Myr with (Fig. 2A, 2B). A 41-kyr filtered sea-level signal displays long-term (1 Myr)  
108 amplitude modulation of obliquity forcing until  $\sim$ 1 Ma, with lowest coherence between both  
109 occurring during intervals of lower amplitude variations (i.e., nodes) (Fig. 2C, 2D). The increase  
110 in amplitude after the first node centered on 3.3-3.1 Ma may reflect a threshold response to the  
111 increase in obliquity forcing that led to the intensification of NH glaciation (29). The below-present

112 highstands and reduced variability between 2.25 Ma and 1.45 Ma (Fig. 1F) are associated with the  
113 second node at ~1.8 Ma (Fig. 2C, 2D). The decrease in amplitude after the third node ~1 Ma  
114 reflects the decrease in size of 41-kyr ice sheets relative to those that characterized the Pleistocene  
115 prior to 1 Ma, with large ice sheets now occurring less frequently (every ~100 kyr) (Fig. 1C).

116 The evolution of changes in sea-level variability over the past 2.5 Myr as measured by sea-  
117 level terminations (defined as the maximum rate of sea-level rise during deglaciations) (Fig. 3D)  
118 shares the same relationship to obliquity as similarly defined GMST terminations (Figure 3B).  
119 This includes the occurrence of terminations between 2.5 Ma and 1.2 Ma for every (near-)  
120 maximum in obliquity, as previously found with an independent age model (13), except during the  
121 node in obliquity modulation centered on 1.8 Ma (Fig. 2C, 2D) when a small concentration of  
122 precessional variance appears (Figure 3F).

123 Over the past 1.2 Myr, we identify eight intervals (M8-M1) that begin and end with sea-  
124 level terminations associated with rising or peak obliquity (Fig. 3), with good agreement (within  
125 0.5-4 kyr) between the mean ages of terminations during the past 1 Myr derived here and those  
126 derived from radiometric dating (14, 30, 31). Each of the eight intervals brackets 1-2 obliquity  
127 peaks without a corresponding termination (Fig. 3D, 3E), consistent with previous work (13, 32,  
128 33). This low-frequency signal first appears 1.19 Ma during the 72-kyr M8 interval. This pattern  
129 is repeated for the 78-kyr M7 interval between Terminations X (0.87 Ma) and IX (0.79 Ma) and  
130 the 89-kyr M6 interval between Terminations VIII (0.71 Ma) and VII (0.62 Ma), with each of these  
131 two intervals followed by a shorter length interval when a termination accompanies an obliquity  
132 maximum. A similar interval of one skipped obliquity cycle between Terminations X and XII was  
133 inferred from a  $\delta^{18}\text{O}_b$  record (14) but our  $\Delta\text{GMST}$  and GMSL reconstructions show that the  
134 intervening Termination XI was as large as some earlier terminations (Fig. 3B, 3D). Five more

135 intervals with 1-2 skipped obliquity cycles (M5-M1) span all of the past 0.53 Myr except for one  
136 brief 29-kyr interval between M3 and M2 (31) which reflects a temperature and sea-level  
137 oscillation during Marine Isotope Stage 7 associated with the strongest obliquity forcing since 2.5  
138 Ma (Fig. 3C). The average duration of the M7-M1 intervals is  $93.9 \pm 13.4$  kyr, resulting in the “100-  
139 kyr cycle” seen in the late-Pleistocene spectra of  $\Delta$ GMST and GMSL (Fig. 3F) and their rates of  
140 change (Figs. 3B, 3D). One notable difference is that GMSL terminations throughout the  
141 Pleistocene only occur after sea level falls below -80 m followed by the next increase to (near-)  
142 obliquity maxima (Fig. 3E), suggesting that ice sheets become unstable when exceeding this size,  
143 whereas GMST terminations have no comparable temperature threshold.

144 Our reconstruction of Pliocene highstands and the onset of NH glaciation between 4 and 3  
145 Ma is in good agreement with other studies (34-36) including one that subtracted local temperature  
146 from  $\delta^{18}\text{O}_b$  to derive  $\delta^{18}\text{O}_{\text{sw}}$  and sea level as done here (37) (fig. S5). A similar local temperature-  
147 based reconstruction reproduces the intensification of NH glaciation that culminated in a LGM-  
148 like sea-level lowstand at  $\sim 2.5$  Ma (26) (fig. S5) while another reproduces large ice sheets  
149 throughout the Pleistocene (38) (fig. S6E). To first order, the similarity between temperature-based  
150 sea-level reconstructions and our GMSL reconstruction is due to the local temperature  
151 reconstructions being nearly the same as our  $\Delta$ MOT reconstruction (18). Several additional lines  
152 of evidence identify early Pleistocene NH ice sheets that were at or beyond their LGM extents by  
153  $\sim 2.5$  Ma, including well-dated terrestrial (39, 40), marine (41, 42), and geophysical (43) records  
154 (Fig. 1D) and ice-rafted debris records in the North Atlantic (44) and North Pacific (45) oceans  
155 (Fig. 1E), consistent with them being volumetrically as large as at the LGM.

156 In contrast, changes in Pleistocene GMSL inferred from the  $\delta^{18}\text{O}_b$  record (46, 47) (Fig. 1A)  
157 and from several reconstructions derived from it (9, 22, 25, 27, 28) find that the culminating

158 lowstand at 2.5 Ma was only ~40% that of the LGM lowstand. Subsequent lowstands then  
159 remained at a similar intermediate level (~ -50 m) until the MPT when they furthered lowered,  
160 reaching LGM-like levels by 0.8 Ma (fig. S6A-D). Given the robust evidence for spatially  
161 extensive early Pleistocene ice sheets (Fig. 1D, 1E), the associated intermediate-size lowstands  
162 imply low-aspect ratio ice sheets relative to those following the MPT (i.e., on average thinner,  
163 since the ice volume is less but the area the same). This was the basis for the regolith hypothesis  
164 for the MPT (48). We attribute these findings of intermediate-size early Pleistocene ice sheets to  
165 the underlying methods that, by default, preserve the variability of the  $\delta^{18}\text{O}_b$  record, including the  
166 increase in the size of glaciations during the MPT, with a further underestimation of early  
167 Pleistocene glaciations due to the lack of accounting for the long-term decrease in GMST on  $\delta^{18}\text{O}_i$   
168 (Fig. S3) (see the supplementary materials, section 1). Lastly, the good agreement between our  
169 reconstruction and all those that cover the past 0.8 Myr (fig. S7) suggest a robust understanding of  
170 GMSL since the MPT.

### 171 **Towards resolving the paradox of large early Pleistocene ice sheets**

172 A well-known paradox posed by early Pleistocene GMSL reconstructions is that their  
173 spectra are dominated by 41-kyr variability despite peak summer insolation being dominated by  
174 precession (49). Coupled climate and ice-sheet models have reproduced NH ice-sheet 41-kyr  
175 variability when accounting for albedo feedbacks, the integrated summer insolation forcing, and  
176 thin ice sheets with ablation zones that remained poleward of 60°N (33, 50, 51). However, such  
177 ice sheets are inconsistent with the geologic evidence for their southern margins in North America  
178 reaching 39°N during the early Pleistocene (Fig. 1D) (39, 52) and they would not dominate the  
179 variability seen in our reconstruction. Another hypothesis proposes that higher early Pleistocene  
180 temperatures caused the response of the ANT ice sheet to precessional forcing to be out of phase

181 with NH ice sheets, thus cancelling the 23-kyr signal in sea-level records (53). However,  
182 hemispheric  $\Delta$ SST reconstructions show a dominant in-phase 41-kyr signal with virtually no  
183 precessional power (21) and this hypothesis cannot account for the large obliquity-driven NH ice  
184 sheets in our reconstruction which had about twice the volume as modeled by Ref. (53).

185 We propose that obliquity forced variations in the Southern Ocean carbon cycle during the  
186 early Pleistocene caused dominant  $[\text{CO}_2]_{\text{atm}}$  variability at this frequency (54). At the same time,  
187 the dominant 41-kyr signal of Southern Ocean SSTs and the temperature effects of related changes  
188 in the position of the sea-ice edge would have been advected through the shallow meridional  
189 circulation and upwelled in the equatorial Pacific (55, 56), where they combined with the SST  
190 variability from  $\text{CO}_2$  forcing to induce the observed dominant 41-kyr SST signal at these low  
191 latitudes (21, 57). Observations (58) and modeling (59) show that changes in equatorial Pacific  
192 SSTs can strongly influence NH ice-sheet surface mass balance (SMB), with the ice-sheet changes  
193 then potentially acting as a positive feedback on equatorial Pacific SSTs (60).

194 Our results pose another dimension to this paradox in showing that large ice sheets existed  
195 throughout the Pleistocene while glacial GMSTs underwent a  $\sim 6^{\circ}\text{C}$  long-term cooling (Figs. 1B,  
196 1C), with polar amplification causing an even greater amount of cooling experienced by the high-  
197 latitude ice sheets (21). This relationship is further complicated by the strong effect that ice sheets  
198 have on their own local climate (61). We propose that the effects of higher early Pleistocene  
199 temperatures on ice-sheet SMB were mitigated by an associated increase in high-latitude  
200 precipitation directly from warming (Clausius-Clapeyron relationship) as well as from latitudinal  
201 shifts in the westerlies as SST gradients changed (62). We can then infer that while cooling  
202 decreased accumulation over glaciated regions, the same cooling reduced surface ablation and thus  
203 caused SMB to remain positive. Similar transient relationships between other factors affecting

204 SMB such as the influence of clouds on ice-sheet surface energy balance (63, 64) or terrestrial  
205 ecosystem emissions and atmospheric chemistry (65) can also be considered. If involved, changes  
206 in these transient feedbacks with global cooling continued to combine in such a way as to induce  
207 ice-sheet SMB that supported the growth of large ice sheets and then maintained their presence in  
208 response to obliquity forcing, suggesting an extraordinary balancing act that allowed the inception  
209 and growth of ice sheets to their maximum size under a range of GMST and  $[CO_2]_{atm}$ .

210 To explore this issue further, we conducted several experiments with the GENESIS V3.0  
211 climate model (66, 67) to examine the sensitivity of early Pleistocene NH ice-sheet SMB to orbits,  
212 atmospheric  $CO_2$ , and ice-sheet height (see supporting information, section 4, Table S1). We first  
213 assessed our modeling strategy by running an experiment with LGM boundary conditions and  
214 found that the simulated NH ice sheets are in or have positive SMB. Our sensitivity experiments  
215 for early Pleistocene ice sheets included various combinations of orbits corresponding to low (at  
216 2.165 Ma) and high (at 2.145 Ma) obliquity (68),  $[CO_2]_{atm}$  of 200 and 300 ppmv that covers much  
217 of the range suggested by proxies (69), and three ice-sheet configurations that assess sensitivity to  
218 ice-sheet height for a given LGM area (Table S1). Our results suggest that early Pleistocene ice  
219 sheets that were larger than LGM ice sheets could have been in SMB with low obliquity and  
220  $[CO_2]_{atm}$  of 300 ppmv. SMB becomes more negative as ice-sheet height is lowered to LGM values  
221 unless there is a compensatory decrease in  $[CO_2]_{atm}$ . No decrease in  $[CO_2]_{atm}$  within the range of  
222 our current understanding of its Pleistocene variability could support the low-aspect-ratio ice  
223 sheets in SMB inferred by the regolith hypothesis (48).

224 We thus conclude that the extra height of the early Pleistocene ice sheets relative to the  
225 LGM was critical to them being in SMB during glaciations. Given our finding that the large ice  
226 sheets shared a common size threshold throughout the Pleistocene equivalent to sea level below -

227 80 m that, when exceeded, triggered ice-sheet instabilities that culminated in a termination (Fig.  
228 3E), we have narrowed this aspect of the paradox to understanding how different boundary  
229 conditions and feedbacks may have contributed to the inception and growth of the early  
230 Pleistocene ice sheets.

231 **Towards resolving the paradox of the middle Pleistocene transition and the origin of the**  
232 **~100-kyr cycle**

233 The longstanding MPT paradox relates to the increase in amplitude and decrease in  
234 frequency of GMSL variability during the MPT in the absence of any corresponding change in  
235 orbital forcing (4). Our finding that large ice sheets existed throughout the Pleistocene, however,  
236 challenges several key aspects of their behavior that are usually invoked to explain this paradox:  
237 (i) that large ice sheets developed during the MPT in response to long-term changes internal to the  
238 climate system (4, 48, 70-75), (ii) that the time constant for growth of large ice sheets is  
239 significantly longer than for ice-sheet decay, giving rise to ~100-kyr cycles (76-78), and (iii) that  
240 through their large inertia and influence on climate, the large ice sheets drove the ~100-kyr cycle  
241 in the rest of the climate system (8, 79, 80).

242 We first note that because pre-MPT ice sheets were as large as those after the MPT, their  
243 albedo forcing should have remained largely the same throughout the Pleistocene and thus cannot  
244 explain the large increase in orbital-scale GMST variability during the MPT (Fig. 1B). Instead, we  
245 attribute that increase to an increase in CO<sub>2</sub> variability associated with changes in the Southern  
246 Ocean carbon cycle. Ref. (21) proposed that the gradual cooling of the Southern Ocean through  
247 the early Pleistocene initiated the MPT in GMST at ~1.5 Ma when average extratropical Southern  
248 Hemisphere SSTs first decreased below pre-industrial, increasing the sensitivity of sea ice to the  
249 dominant obliquity forcing at these high latitudes. Increased cooling of the Southern Hemisphere

250 also led to an equatorward shift of the westerly winds (81), an increase in dust flux to the Southern  
251 Ocean (82), and greater stratification of surface waters (83). Through their impacts on the Southern  
252 Ocean carbon cycle (81, 82, 84-87), these changes increased carbon storage during glaciations,  
253 thus increasing obliquity-scale variability of  $[\text{CO}_2]_{\text{atm}}$  and GMST. However, a further decrease and  
254 then stabilization of Southern Ocean  $\Delta\text{SSTs}$  at the end of the MPT  $\sim 0.9$  Ma then muted the  
255 response of the Southern Ocean carbon cycle to obliquity forcing that may have dominated  
256  $[\text{CO}_2]_{\text{atm}}$  variability during the early Pleistocene, with an attendant large decrease in the  
257 concentration of 41-kyr variance in  $[\text{CO}_2]_{\text{atm}}$  and GMST (21).

258 We similarly attribute the decrease in large-ice-sheet 41-kyr variance across the MPT (Fig.  
259 2A, 2B) to modulation of obliquity forcing by the newly established decrease in  $[\text{CO}_2]_{\text{atm}}$  and  
260 GMST variance. Specifically, prior to reaching their maximum size at the end of each of the M  
261 intervals, ice-sheet response to low obliquity was modulated by periods of higher  $[\text{CO}_2]_{\text{atm}}$  and  
262 GMST, and vice versa, with times of maximum ice-sheet growth only occurring when the next  
263 obliquity low combined with low  $[\text{CO}_2]_{\text{atm}}$  and GMST (Figs. 4A, 4B, 4C). The initial retreat of  
264 large ice sheets in response to the next increase in obliquity then triggered a sequence of events  
265 and feedbacks leading to a termination every  $\sim 100$  kyr (31). Among these feedbacks are large-ice-  
266 sheet instabilities that sustained ice-sheet retreat (8, 77, 88-91) which, through its influence on the  
267 Atlantic meridional overturning circulation, induced warming of the Southern Ocean with an  
268 associated retreat of sea ice, deterioration of the Southern Ocean halocline, and poleward shift in  
269 the westerlies. These changes then led to the release of  $\text{CO}_2$  from the deep ocean (87) which  
270 combined with obliquity (Fig. 4D) to fully deglaciate NH ice sheets and usher in the next  
271 interglaciation.

272 Contrasting temperature and ice-sheet responses to CO<sub>2</sub> forcing over the past 0.8 Myr are  
273 clearly expressed in their variance spectra, with a dominant ~100-kyr cycle in GMST (21) that is  
274 shared by CO<sub>2</sub> (fig. S9A) whereas the concentration of GMSL variance is nearly equally  
275 distributed between 41 kyr and ~100 kyr (Fig. 2B, fig. S9B). Insofar as the variance characteristics  
276 of GMST are shared by GMSST, MOT, and thus δ<sup>18</sup>O<sub>T</sub> (92) and those of GMSL are shared by  
277 δ<sup>18</sup>O<sub>sw</sub>, we can similarly evaluate the relative contributions of δ<sup>18</sup>O<sub>T</sub> and δ<sup>18</sup>O<sub>sw</sub> to the variance of  
278 the δ<sup>18</sup>O<sub>b</sub> record since the MPT. The δ<sup>18</sup>O<sub>b</sub> record has long been used to argue that the dominant  
279 post-MPT ~100-kyr signal in that record (Fig. 5A) is from ice-sheet dynamics (8, 14, 93-95), but  
280 our results show that its origin is largely in the δ<sup>18</sup>O<sub>T</sub> component due to changes in the carbon  
281 cycle (Fig. 5B), as first recognized by Ref. (75). Overall, however, terminations present in both  
282 δ<sup>18</sup>O<sub>T</sub> and δ<sup>18</sup>O<sub>sw</sub> were set by the threshold of when ice sheets exceeded a limiting size beyond  
283 which they responded nonlinearly to obliquity forcing and helped drive a termination. This  
284 threshold was reached for nearly every obliquity cycle of the Pleistocene prior to the MPT (Fig.  
285 3D, 3E). Afterward, the development of the ~100-kyr cycle arising from the long-term cooling  
286 enhanced the ability of the Southern Ocean carbon cycle to sequester CO<sub>2</sub> and modulate the  
287 response of δ<sup>18</sup>O<sub>T</sub> and δ<sup>18</sup>O<sub>sw</sub> to obliquity forcing until the growth of the next large ice sheet.

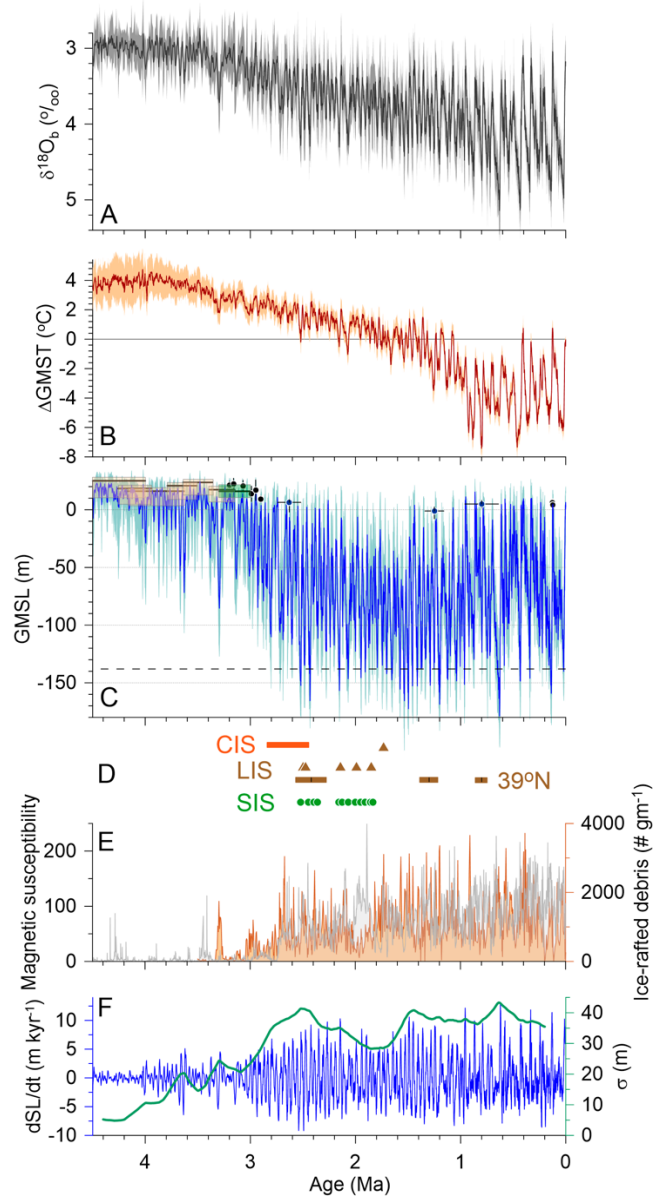
## 288 **Conclusions**

289 We find that between 4.5 and 3 Ma, sea-level highstands remained ~20 m above present  
290 suggesting large decreases in AIS and GrIS volume relative to today. Beginning at 4 Ma, sea-level  
291 lowstands began to episodically extend below present by as much as -50 to -80 m suggesting the  
292 onset of Northern Hemisphere (NH) glaciation. Sustained intensification of NH glaciation  
293 occurred from 3 Ma to 2.5 Ma, with highstands decreasing to near-modern levels while lowstands

294 decreased to levels comparable to or lower than the Last Glacial Maximum (LGM) lowstand ~21  
295 ka that continued throughout much of the Pleistocene.

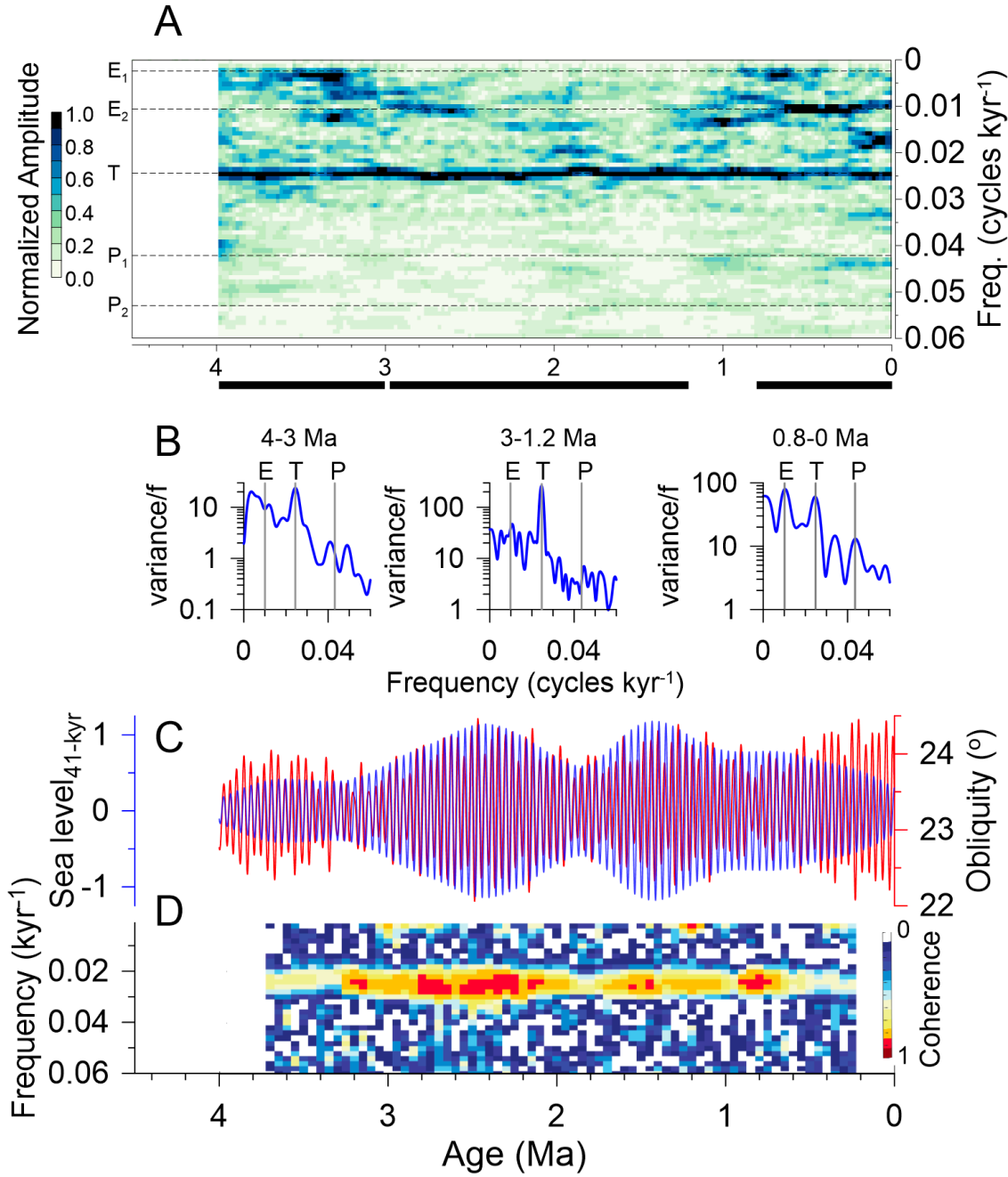
296 Our finding that large ice sheets existed throughout the Pleistocene modifies as well as  
297 adds several fundamental challenges to our understanding of ice sheet-climate interactions and  
298 their joint responses to external forcing. Underlying each of these challenges is the fact that the  
299 dominant orbital-scale GMSL variability and its changes over the past 3 Myr is not the one that  
300 would be predicted by the associated orbital forcing, suggesting internal feedbacks of the climate  
301 system that we propose are largely driven by changes in the Southern Ocean carbon cycle and their  
302 effect on  $[\text{CO}_2]_{\text{atm}}$  and GMST. High-resolution ice-core  $\text{CO}_2$  records that extend beyond 0.8 Ma  
303 are needed to test our hypotheses. Finally, the presence of large ice sheets throughout the MPT  
304 indicates that the hypothesis of regolith removal to explain the change in ice-sheet sensitivity to  
305 orbital forcing (5, 48) can be rejected.

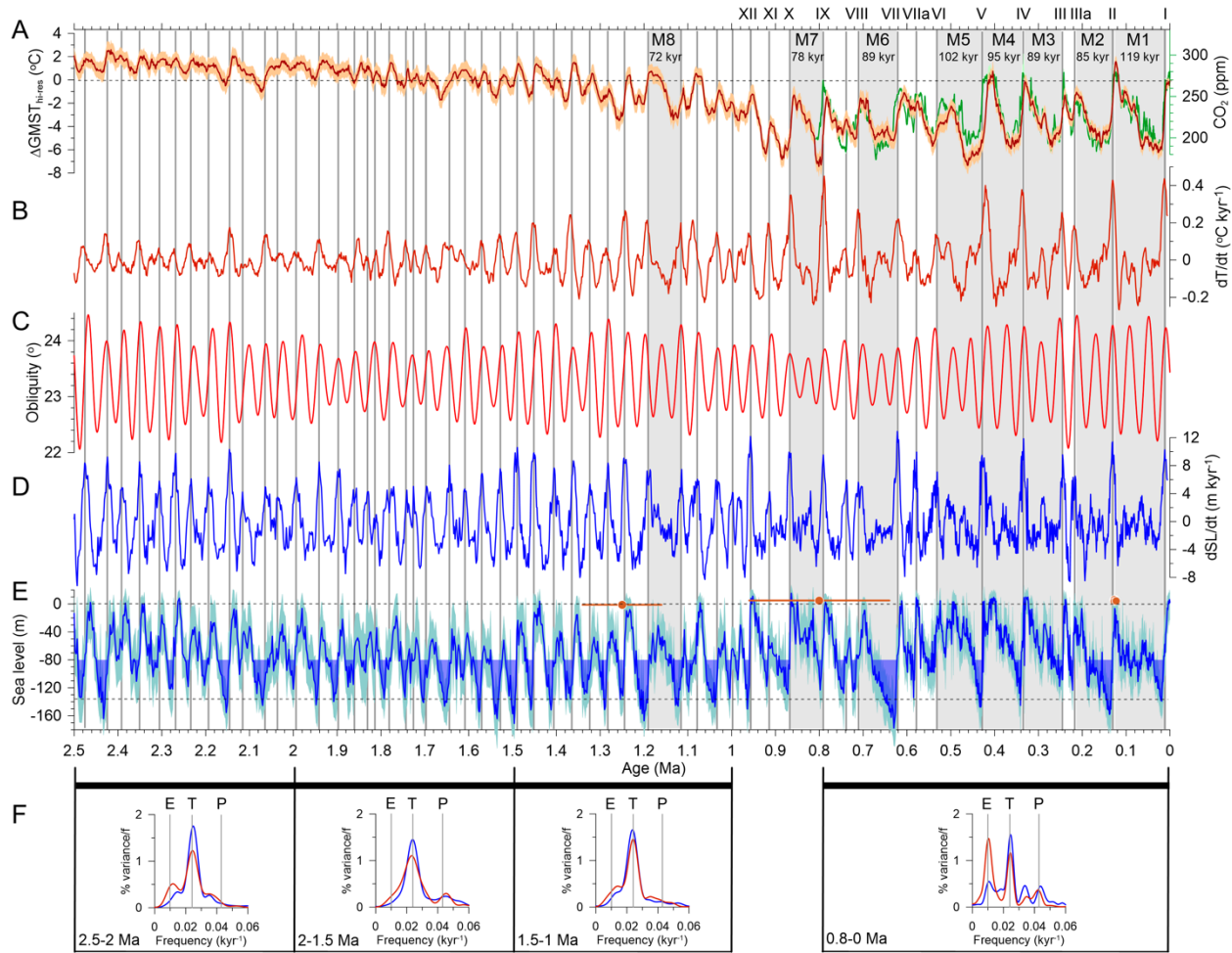
306



307

308 **Fig. 1. Global mean temperature and sea-level changes over the past 4.5 Myr.** (A) Prob-stack  
 309  $\delta^{18}\text{O}_b$  record (12). (B) Global mean surface temperature difference ( $\Delta\text{GMST}$ ) (brick red with  $1\sigma$   
 310 uncertainty) referenced to PI. (C) Global mean sea level (GMSL) (blue line with  $1\sigma$  uncertainty).  
 311 Also shown are published Pliocene (34-36) and Pleistocene (96, 97) sea-level highstands. Dashed  
 312 horizontal line is referenced to the LGM lowstand (-130 m). (D) Geologic evidence of extensive  
 313 margins of early-to-middle Pleistocene Cordilleran Ice Sheet (CIS, orange symbols) (40),  
 314 Laurentide Ice Sheet records at 39°N (LIS, brown symbols) (39, 41), and Scandinavian Ice Sheet  
 315 (SIS, green symbols) (43). Newer evidence suggests a more-limited extent of the SIS in the North  
 316 Sea prior to 1.1 Ma (98) than inferred by Ref. (43), but the difference in extent, and its contribution  
 317 to GMSL, is negligible. (E) Records of ice-rafted debris from the North Pacific (gray) (45) and  
 318 Nordic Seas (orange) (44). (F) Rate of change (12-kyr running average) (dark blue line) and  
 319 standard deviation ( $\sigma$ , 200-kyr centered) (green line) of GMSL.

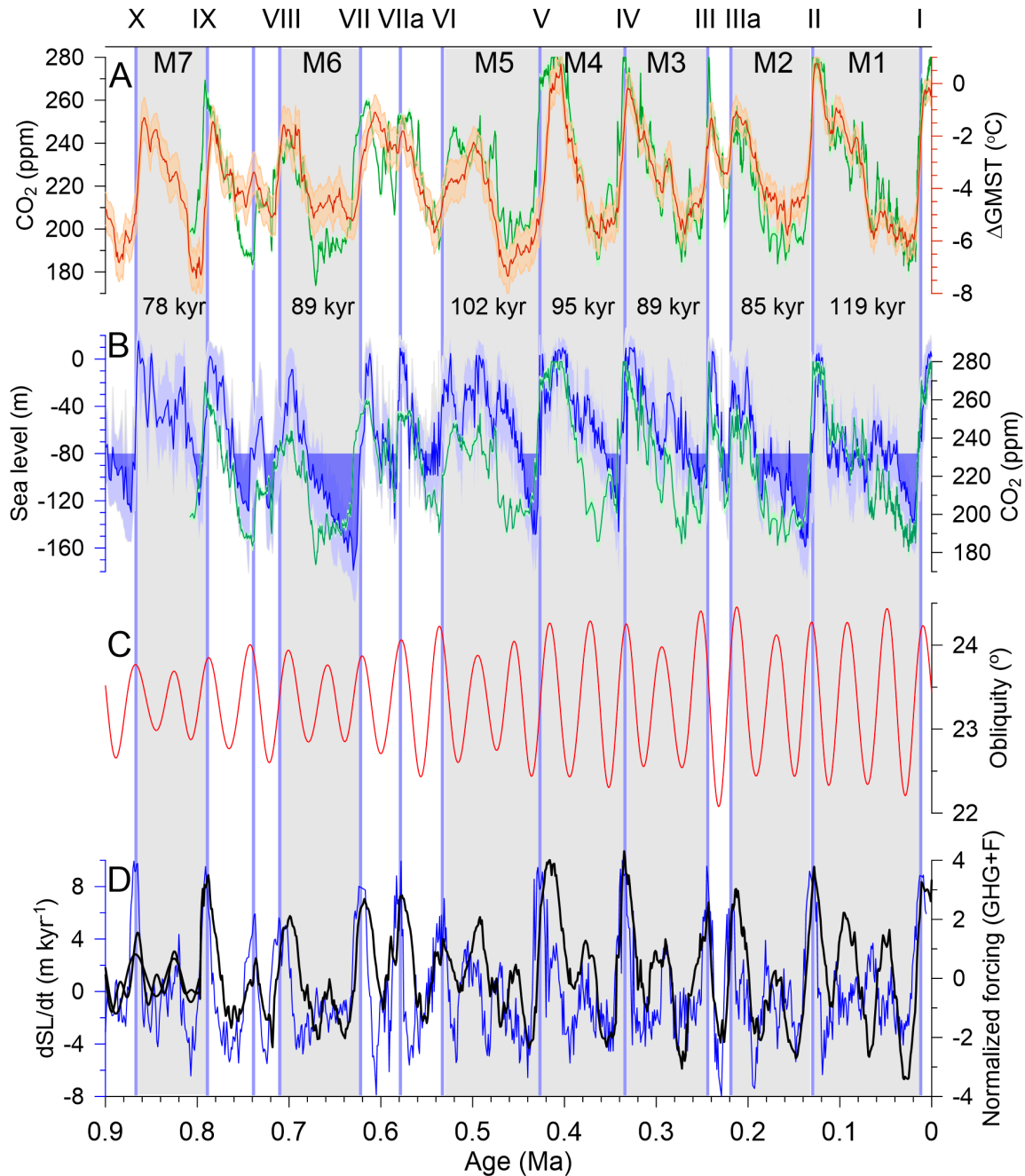




330

331

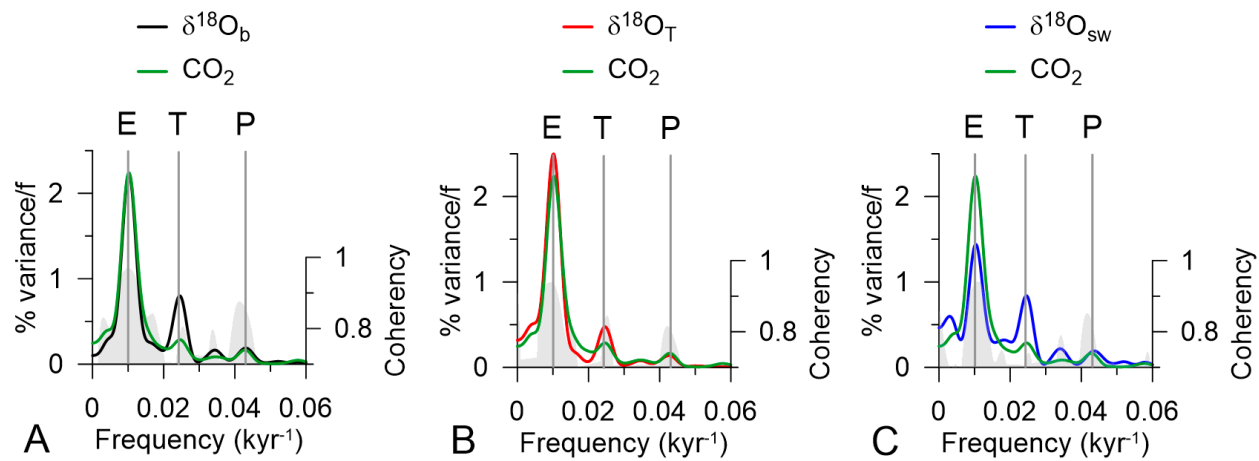
332 **Fig. 3. Global temperature and sea-level changes over the past 2.5 Myr.** (A) Global mean  
 333 temperature change ( $\Delta\text{GMST}$ ) (brick red with  $1\sigma$  uncertainty,) referenced to PI, and  
 334 atmospheric CO<sub>2</sub> (green) (99) placed on the AICC2023 chronology (100). (B) Rate of change of  
 335  $\Delta\text{GMST}$ . (C) Obliquity (68). (D) Rate of change of global mean sea level (GMSL) (12-kyr running  
 336 average), whose maxima are highlighted by vertical lines across (A-E). (E) Global mean sea level.  
 337 Sea-level threshold of -80 m that, when exceeded, is followed by a termination upon next increase  
 338 in obliquity (see text) is shown by filled blue sea-level intervals. Dashed horizontal lines  
 339 correspond to present (0 m) and LGM (-130 m) sea levels. Brick-red symbols with  $1\sigma$  age  
 340 uncertainty are published Pleistocene sea-level highstands (96, 97). (F) Spectral density of rate of  
 341 change of  $\Delta\text{GMST}$  (brick red) and GMSL (blue) for four periods corresponding to horizontal black  
 342 bars shown in (E). Eccentricity (E, 100-kyr), tilt (T, 41-kyr) and precession (P, 23-kyr) frequency  
 343 bands noted by vertical lines.  
 344



345

346 **Fig. 4. Assessing the origin of the ~100-kyr cycle.** (A) Global mean surface temperature change  
 347 (ΔGMST) (brick red) referenced to PI, and atmospheric CO<sub>2</sub> (green) (99) both with 1 $\sigma$  uncertainty.  
 348 (B) Global mean sea level (GMSL) (blue) and atmospheric CO<sub>2</sub> (green) (99), both with 1 $\sigma$   
 349 uncertainty. (C) Obliquity (68). (D) Rate of change of GMSL (blue) compared to a normalized  
 350 forcing function F (GHG+F) (101) that combines normalized atmospheric CO<sub>2</sub> from the Antarctic  
 351 ice-core record over the past 0.8 Myr (black) (99) placed on the AICC2023 chronology (100) and  
 352 normalized obliquity. Note that there is no significant improvement in the correlation between rate  
 353 of change of GMSL and a forcing function that combines various proportions of precession and  
 354 obliquity (5:95, 25:75, 50:50).  
 355

356



357

358 **Fig. 5. Spectral density of the  $\delta^{18}\text{O}_b$  record, its components, and atmospheric  $\text{CO}_2$  for past**  
 359 **0.8 Myr.** (A) Spectral density (normalized variance) of the Prob-stack  $\delta^{18}\text{O}_b$  record (12) and  
 360 atmospheric  $\text{CO}_2$  (green) (99). (B) Spectral density (normalized variance) of the temperature  
 361 component ( $\delta^{18}\text{O}_T$ ) of the  $\delta^{18}\text{O}_b$  record (18) and atmospheric  $\text{CO}_2$  (green) (99). (C) Spectral density  
 362 (normalized variance) of the seawater component ( $\delta^{18}\text{O}_{\text{sw}}$ ) of the  $\delta^{18}\text{O}_b$  record (18) and  
 363 atmospheric  $\text{CO}_2$  (green) (99).

364

365 **REFERENCES AND NOTES**

366

367 1. T. Westerhold *et al.*, An astronomically dated record of Earth's climate and its  
368 predictability over the last 66 million years. *Science* **369**, 1383-1387 (2020).

369 2. J. Zachos, M. Pagani, L. Sloan, E. Thomas, K. Billups, Trends, rhythms, and aberrations  
370 in global climate 65 Ma to present. *Science* **292**, 686-693 (2001).

371 3. N. J. Shackleton, N. D. Opdyke, R. M. Cline, J. D. Hays, Eds. (Geological Society of  
372 America Memoir, Boulder, CO, 1976), vol. 145, pp. 449-464.

373 4. N. G. Pisias, T. C. Moore, Jr., The evolution of Pleistocene climate: a time series approach.  
374 *Earth and Planetary Science Letters* **52**, 450-458 (1981).

375 5. P. U. Clark *et al.*, The middle Pleistocene transition: Characteristics, mechanisms, and  
376 implications for long-term changes in atmospheric PCO<sub>2</sub>. *Quaternary Science Reviews* **25**,  
377 3150-3184 (2006).

378 6. J. D. Hays, J. Imbrie, N. J. Shackleton, Variations in the Earth's orbit: Pacemaker of the ice  
379 ages. *Science* **194**, 1121-1132 (1976).

380 7. J. Imbrie *et al.*, On the structure and origin of major glaciation cycles 1. Linear responses  
381 to Milankovitch forcing. *Paleoceanography* **7**, 701-738 (1992).

382 8. J. Imbrie *et al.*, On the structure and origin of major glaciation cycles. 2. The 100,000-year  
383 cycle. *Paleoceanography* **8**, 699-735 (1993).

384 9. J. Hansen, M. Sato, G. Russell, P. Kharecha, Climate sensitivity, sea level and atmospheric  
385 carbon dioxide. *Philosophical Transactions of the Royal Society A-Mathematical Physical  
386 and Engineering Sciences* **371**, 10.1098/rsta.2012.0294 (2013).

387 10. N. G. Pisias *et al.*, High resolution stratigraphic correlation of benthic oxygen isotopic  
388 records spanning the last 300,000 years. *Marine Geology*, **56**, 119-136 (1984).

389 11. L. E. Lisiecki, M. E. Raymo, A Pliocene-Pleistocene stack of 57 globally distributed  
390 benthic  $\delta^{18}\text{O}$  records. *Paleoceanography* **20**, 2004PA001071 (2005).

391 12. S. Ahn, D. Khider, L. E. Lisiecki, C. E. Lawrence, A probabilistic Pliocene–Pleistocene  
392 stack of benthic  $\delta^{18}\text{O}$  using a profile hidden Markov model. *Dynamics and Statistics of the  
393 Climate System* **2**, 1-16 (2017).

394 13. P. Huybers, Glacial variability over the last two million years: an extended depth-derived  
395 age model, continuous obliquity pacing, and the Pleistocene progression. *Quaternary  
396 Science Reviews* **26**, 37-55 (2007).

397 14. P. Bajo *et al.*, Persistent influence of obliquity on ice age terminations since the Middle  
398 Pleistocene transition. *Science* **367**, 1235-1239 (2020).

399 15. M. E. Raymo, R. Kozdon, D. Evans, L. Lisiecki, H. L. Ford, The accuracy of mid-Pliocene  
400  $\delta^{18}\text{O}$ -based ice volume and sea level reconstructions. *Earth-Science Reviews* **177**, 291-302  
401 (2018).

402 16. D. P. Schrag, Effects of diagenesis on the isotopic record of late Paleogene tropical sea  
403 surface temperatures. *Chemical Geology* **161**, 215-224 (1999).

404 17. H. J. Spero, J. Bijma, D. W. Lea, B. E. Bemis, Effect of seawater carbonate concentration  
405 on foraminiferal carbon and oxygen isotopes. *Nature* **390**, 497-500 (1997).

406 18. P. U. Clark *et al.*, Mean ocean temperature change and decomposition of the benthic  $\delta^{18}\text{O}$   
407 record over the last 4.5 Myr. *EGUsphere* **2024**, 1-41 (2024).

408 19. M. J. Winnick, J. K. Caves, Oxygen isotope mass-balance constraints on Pliocene sea level  
409 and East Antarctic Ice Sheet stability. *Geology* **43**, 879-882 (2015).

410 20. E. Gasson, R. M. DeConto, D. Pollard, Modeling the oxygen isotope composition of the  
411 Antarctic ice sheet and its significance to Pliocene sea level. *Geology* **44**, 827-830 (2016).

412 21. P. U. Clark, J. D. Shakun, Y. Rosenthal, P. Köhler, P. J. Bartlein, Global and regional  
413 temperature change over the last 4.5 million years. *Science* **383**, 884-890 (2024).

414 22. K. G. Miller *et al.*, Cenozoic sea-level and cryospheric evolution from deep-sea  
415 geochemical and continental margin records. *Science Advances* **6**, (2020).

416 23. J. D. Shakun, D. W. Lea, L. E. Lisiecki, M. E. Raymo, An 800-kyr record of global surface  
417 ocean delta O-18 and implications for ice volume-temperature coupling. *Earth and*  
418 *Planetary Science Letters* **426**, 58-68 (2015).

419 24. C. Waelbroeck *et al.*, Sea-level and deep water temperature changes derived from benthic  
420 foraminifera isotopic records. *Quaternary Science Reviews* **21**, 295-305 (2002).

421 25. S. L. Bates, M. Siddall, C. Waelbroeck, Hydrographic variations in deep ocean temperature  
422 over the mid-Pleistocene transition. *Quaternary Science Reviews* **88**, 147-158 (2014).

423 26. K. A. Jakob *et al.*, A new sea-level record for the Neogene/Quaternary boundary reveals  
424 transition to a more stable East Antarctic Ice Sheet. *Proceedings of the National Academy*  
425 *of Sciences of the United States of America* **117**, 30980-30987 (2020).

426 27. E. J. Rohling *et al.*, Comparison and synthesis of sea-level and deep-sea temperature  
427 variations over the past 40 million years. *Reviews of Geophysics* **60**, e2022RG000775  
428 (2022).

429 28. E. J. Rohling *et al.*, Sea level and deep-sea temperature reconstructions suggest quasi-stable  
430 states and critical transitions over the past 40 million years. *Science Advances* **7**, eabf5326  
431 (2021).

432 29. M. A. Maslin, X. S. Li, M. F. Loutre, A. Berger, The contribution of orbital forcing to the  
433 progressive intensification of Northern Hemisphere glaciation. *Quaternary Science*  
434 *Reviews* **17**, 411-426 (1998).

435 30. H. Cheng *et al.*, Ice Age Terminations. *Science* **326**, 248-252 (2009).

436 31. H. Cheng *et al.*, The Asian monsoon over the past 640,000 years and ice age terminations.  
437 *Nature* **534**, 640-646 (2016).

438 32. P. C. Tzedakis, M. Crucifix, T. Mitsui, E. W. Wolff, A simple rule to determine which  
439 insolation cycles lead to interglacials. *Nature* **542**, 427-432 (2017).

440 33. P. Köhler, R. S. W. van de Wal, Interglacials of the Quaternary defined by northern  
441 hemispheric land ice distribution outside of Greenland. *Nature Communications* **11**,  
442 11:5124 (2020).

443 34. O. A. Dumitru *et al.*, Constraints on global mean sea level during Pliocene warmth. *Nature*  
444 **574**, 233-236 (2019).

445 35. K. G. Miller *et al.*, High tide of the warm Pliocene: Implications of global sea level for  
446 Antarctic deglaciation. *Geology* **40**, 407-410 (2012).

447 36. F. D. Richards *et al.*, Geodynamically corrected Pliocene shoreline elevations in Australia  
448 consistent with midrange projections of Antarctic ice loss. *Science Advances* **9**, (2023).

449 37. G. S. Dwyer, M. A. Chandler, Mid-Pliocene sea level and continental ice volume based on  
450 coupled benthic Mg/Ca palaeotemperatures and oxygen isotopes. *Philosophical*  
451 *Transactions of the Royal Society A-Mathematical Physical and Engineering Sciences* **367**,  
452 157-168 (2009).

453 38. S. Sosdian, Y. Rosenthal, Deep-sea temperature and ice volume changes across the  
454 Pliocene-Pleistocene climate transitions. *Science* **325**, 306-310 (2009).

455 39. G. Balco, C. W. Rovey, Absolute chronology for major Pleistocene advances of the  
456 Laurentide Ice Sheet. *Geology* **38**, 795-798 (2010).

457 40. A. J. Hidy, J. C. Gosse, D. G. Froese, J. D. Bond, D. H. Rood, A latest Pliocene age for the  
458 earliest and most extensive Cordilleran Ice Sheet in northwestern Canada. *Quaternary  
459 Science Reviews* **61**, 77-84 (2013).

460 41. J. D. Shakun, M. E. Raymo, D. W. Lea, An early Pleistocene Mg/Ca- $\delta^{18}\text{O}$  record from the  
461 Gulf of Mexico: Evaluating ice sheet size and pacing in the 41-kyr world.  
462 *Paleoceanography* **31**, 1011-1027 (2016).

463 42. K. Blake-Mizen *et al.*, Southern Greenland glaciation and Western Boundary Undercurrent  
464 evolution recorded on Eirik Drift during the late Pliocene intensification of Northern  
465 Hemisphere glaciation. *Quaternary Science Reviews* **209**, 40-51 (2019).

466 43. B. R. Rea *et al.*, Extensive marine-terminating ice sheets in Europe from 2.5 million years  
467 ago. *Science Advances* **4**, eaar8327 (2018).

468 44. E. Jansen, T. Fronval, F. Rack, J. E. T. Channell, Pliocene-Pleistocene ice rafting history  
469 and cyclicity in the Nordic Seas during the last 3.5 Myr. *Paleoceanography* **15**, 709-721  
470 (2000).

471 45. G. H. Haug, D. M. Sigman, R. Tiedemann, T. F. Pedersen, M. Sarnthein, Onset of  
472 permanent stratification in the subarctic Pacific Ocean. *Nature* **401**, 779-782 (1999).

473 46. N. J. Shackleton, N. D. Opdyke, Oxygen isotope and paleomagnetic evidence for early  
474 Northern Hemisphere glaciation. *Nature* **270**, 216-219 (1977).

475 47. M. E. Raymo, The initiation of Northern Hemisphere glaciation. *Annual Review of Earth  
476 Planetary Sciences*, **22**, 353-383 (1994).

477 48. P. U. Clark, D. Pollard, Origin of the middle Pleistocene transition by ice sheet erosion of  
478 regolith. *Paleoceanography* **13**, 1-9 (1998).

479 49. M. E. Raymo, K. Nisancioglu, The 41 kyr world: Milankovitch's other unsolved mystery.  
480 *Paleoceanography* **18**, 2002PA000791 (2003).

481 50. P. Huybers, E. Tziperman, Integrated summer insolation forcing and 40,000-year glacial  
482 cycles: The perspective from an ice-sheet/energy-balance model. *Paleoceanography* **23**,  
483 PA1208 (2008).

484 51. C. R. Tabor, C. J. Poulsen, D. Pollard, How obliquity cycles powered early Pleistocene  
485 global ice-volume variability. *Geophysical Research Letters* **42**, 1871-1879 (2015).

486 52. J. Boellstorff, North American Pleistocene stages reconsidered in light of probably  
487 Pliocene-Pleistocene continental glaciation. *s* **202**, 305-307 (1978).

488 53. M. E. Raymo, L. E. Lisiecki, K. H. Nisancioglu, Plio-Pleistocene ice volume, Antarctic  
489 climate, and the global delta O-18 record. *Science* **313**, 492-495 (2006).

490 54. K. A. Dyez, B. Honisch, G. A. Schmidt, Early Pleistocene Obliquity-Scale pCO<sub>2</sub>  
491 Variability at similar to 1.5 Million Years Ago. *Paleoceanography and Paleoclimatology*  
492 **33**, 1270-1291 (2018).

493 55. Z. Liu, H. Yang, Extratropical control of tropical climate, the atmospheric bridge and  
494 oceanic tunnel. *Geophysical Research Letters* **30**, 1-4 (2003).

495 56. S. Y. Lee, C. J. Poulsen, Sea ice control of Plio-Pleistocene tropical Pacific climate  
496 evolution. *Earth and Planetary Science Letters* **248**, 253-262 (2006).

497 57. T. D. Herbert, L. C. Peterson, K. T. Lawrence, Z. Liu, Tropical ocean temperatures over  
498 the past 3.5 million years. *Science* **328**, 1530-1534 (2010).

499 58. P. Huybers, P. Molnar, Tropical cooling and the onset of North American glaciation.  
500 *Climate of the Past* **3**, 549-557 (2007).

501 59. P. U. Clark, S. W. Hostetler, N. G. Pisias, A. Schmittner, K. J. Meissner, in *Ocean*  
502 *Circulation: Mechanisms and Impacts*, A. Schmittner, J. Chiang, S. Hemming, Eds.  
503 (American Geophysical Union, Geophysical Monograph, 2007), vol. 173, pp. 209-246.

504 60. M. P. Erb, C. S. Jackson, A. J. Broccoli, Using Single-Forcing GCM Simulations to  
505 Reconstruct and Interpret Quaternary Climate Change. *Journal of Climate* **28**, 9746-9767  
506 (2015).

507 61. J. Fyke, O. Sergienko, M. Lofverstrom, S. Price, J. T. M. Lenaerts, An overview of  
508 interactions and feedbacks between ice sheets and the Earth system. *Reviews of Geophysics*  
509 **56**, 361-408 (2018).

510 62. X. Li *et al.*, Mid-Pliocene westerlies from PlioMIP simulations. *Advances in Atmospheric*  
511 *Sciences* **32**, 909-923 (2015).

512 63. S. Hofer, A. J. Tedstone, X. Fettweis, J. L. Bamber, Decreasing cloud cover drives the  
513 recent mass loss on the Greenland Ice Sheet. *Science Advances* **3**, (2017).

514 64. N. Sagoo *et al.*, Observationally Constrained Cloud Phase Unmasks Orbitally Driven  
515 Climate Feedbacks. *Geophysical Research Letters* **48**, (2021).

516 65. N. Unger, X. Yue, Strong chemistry- climate feedbacks in the Pliocene. *Geophysical*  
517 *Research Letters* **41**, 527-533 (2014).

518 66. D. Pollard, S. L. Thompson, Climate and ice-sheet mass balance at the Last Glacial  
519 Maximum from GENESIS version 2 global climate model. *Quaternary Science Reviews*  
520 **16**, 841-863 (1997).

521 67. S. L. Thompson, D. Pollard, Greenland and Antarctic mass balances for present and  
522 doubled atmospheric CO<sub>2</sub> from the GENESIS version-2 global climate model. *Journal of*  
523 *Climate* **10**, 871-900 (1997).

524 68. J. Laskar *et al.*, A long term numerical solution for the insolation quantities of the Earth.  
525 *Astronomy and Astrophysics* **428**, 261-285 (2004).

526 69. P. Köhler, Atmospheric CO<sub>2</sub> concentration based on boron isotopes versus simulations of  
527 the global carbon cycle during the Plio-Pleistocene. *Paleoceanography and*  
528 *Paleoclimatology* **38**, e2022PA004439 (2023).

529 70. A. Berger, X. S. Li, M. F. Loutre, Modelling northern hemisphere ice volume over the last  
530 3 Ma. *Quaternary Science Reviews* **18**, 1-11 (1999).

531 71. M. Willeit, A. Ganopolski, R. Calov, V. Brovkin, Mid-Pleistocene transition in glacial  
532 cycles explained by declining CO<sub>2</sub> and regolith removal. *Science Advances* **5**, eaav7337  
533 (2019).

534 72. E. Tziperman, H. Gildor, On the mid-Pleistocene transition to 100-kyr glacial cycles and  
535 the asymmetry between glaciation and deglaciation times. *Paleoceanography* **18**,  
536 PA000627 (2003).

537 73. P. Huybers, C. Wunsch, Obliquity pacing of the late Pleistocene glacial terminations.  
538 *Nature* **434**, 491-494 (2005).

539 74. T. B. Chalk *et al.*, Causes of ice age intensification across the Mid-Pleistocene Transition.  
540 *Proceedings of the National Academy of Sciences* **114**, 13114-13119 (2017).

541 75. N. J. Shackleton, The 100,000 year Ice-Age cycle identified and found to lag temperature,  
542 carbon dioxides and orbital eccentricity. *Science* **289**, 1897-1902 (2000).

543 76. J. Imbrie, J. Z. Imbrie, Modeling the climatic response to orbital variations. *Science* **207**,  
544 943-953 (1980).

545 77. A. Abe-Ouchi *et al.*, Insolation-driven 100,000-year glacial cycles and hysteresis of ice-  
546 sheet volume. *Nature* **500**, 190-193 (2013).

547 78. D. Pollard, A simple ice sheet model yields realistic 100 kyr glacial cycles. *n* **296**, 334-338  
548 (1982).

549 79. P. U. Clark, R. B. Alley, D. Pollard, Northern Hemisphere ice-sheet influences on global  
550 climate change. *Science* **286**, 1104-1111 (1999).

551 80. W. F. Ruddiman, M. E. Raymo, D. G. Martinson, B. M. Clement, J. Backman, Pleistocene  
552 evolution: northern hemisphere ice sheets and North Atlantic ocean. *Paleoceanography* **4**,  
553 353-412 (1989).

554 81. D. M. Sigman *et al.*, The Southern Ocean during the ice ages: A review of the Antarctic  
555 surface isolation hypothesis, with comparison to the North Pacific. *Quaternary Science  
556 Reviews* **254**, (2021).

557 82. A. Martinez-Garcia *et al.*, Southern Ocean dust-climate coupling over the past four million  
558 years. *Nature* **476**, 312-315 (2011).

559 83. A. P. Hasenfratz *et al.*, The residence time of Southern Ocean surface waters and the  
560 100,000-year ice age cycle. *Science* **363**, 1080-1084 (2019).

561 84. R. Ferrari *et al.*, Antarctic sea ice control on ocean circulation in present and glacial  
562 climates. *Proceedings of the National Academy of Sciences* **111**, 8753-8758 (2014).

563 85. M. F. Jansen, Glacial ocean circulation and stratification explained by reduced atmospheric  
564 temperature. *Proceedings of the National Academy of Sciences* **114**, 45-50 (2017).

565 86. A. Marzocchi, M. F. Jansen, Global cooling linked to increased glacial carbon storage via  
566 changes in Antarctic sea ice. *Nature Geoscience* **12**, 1001-1005 (2019).

567 87. P. Köhler, R. Bintanja, The carbon cycle during the Mid Pleistocene Transition: the  
568 Southern Ocean decoupling hypothesis. *Climate of the Past* **4**, 311-332 (2008).

569 88. D. Pollard, A coupled climate-ice sheet model applied to the Quaternary ice ages. *Journal  
570 of Geophysical Research* **88**, 7705-7718 (1983).

571 89. S. J. Marshall, P. U. Clark, Basal temperature evolution of North American ice sheets and  
572 implications for the 100-kyr cycle. *Geophysical Research Letters* **29**, GL015192 (2002).

573 90. P. U. Clark *et al.*, Oceanic forcing of penultimate deglacial and last interglacial sea-level  
574 rise. *Nature* **577**, 660-664 (2020).

575 91. M. E. Raymo, The timing of major climate terminations. *Paleoceanography* **12**, 577-585  
576 (1997).

577 92. P. U. Clark *et al.*, Mean ocean temperature change and decomposition of the benthic  $d^{18}\text{O}$   
578 record over the last 4.5 Myr. *Climate of the Past*, (in review).

579 93. W. S. Broecker, J. van Donk, Insolation changes, ice volumes, and the O-18 record in deep-  
580 sea cores. *Reviews of Geophysics and Space Physics* **8**, 169-198 (1970).

581 94. N. J. Shackleton, The oxygen isotope stratigraphic record of the Late Pleistocene.  
582 *Philosophical Transactions Royal Society of London* **280B**, 169-182 (1977).

583 95. S. Barker *et al.*, Persistent influence of precession on northern ice sheet variability since  
584 the early Pleistocene. *Science* **376**, 961-+ (2022).

585 96. O. A. Dumitru *et al.*, Sea-level stands from the Western Mediterranean over the past 6.5  
586 million years. *Sci Rep-Uk* **11**, 6681 (2021).

587 97. A. Dutton, J. M. Webster, D. Zwart, K. Lambeck, B. Wohlfarth, Tropical tales of polar  
588 ice: evidence of Last Interglacial polar ice sheet retreat recorded by fossil reefs of the  
589 granitic Seychelles islands. *Quaternary Science Reviews* **107**, 182-196 (2015).

590 98. D. Ottesen, C. L. Batchelor, H. Loseth, H. Brunstad, 3D seismic evidence for a single Early  
591 Pleistocene glaciation of the central North Sea. *Science Advances* **10**, eadq6089 (2024).

592 99. B. Bereiter *et al.*, Revision of the EPICA Dome C CO<sub>2</sub> record from 800 to 600kyr before  
593 present. *Geophysical Research Letters* **42**, 542-549 (2015).

594 100. M. Bouchet *et al.*, The Antarctic Ice Core Chronology 2023 (AICC2023) chronological  
595 framework and associated timescale for the European Project for Ice Coring in Antarctica  
596 (EPICA) Dome C ice core. *Clim. Past* **19**, 2257-2286 (2023).

597 101. P. Huybers, Combined obliquity and precession pacing of late Pleistocene deglaciations.  
598 *Nature* **480**, 229-232 (2011).

599

600

601 **Acknowledgments:** This publication contributed to Beyond EPICA, a project of the European  
602 Union’s Horizon 2020 research and innovation program (Oldest Ice Core).

603 **Funding:**

604 National Science Foundation OPP-2103032 (PUC)  
605 University of Oregon Fund for Faculty Excellence (PB)  
606 National Science Foundation OCE-1810681 (ZL)  
607 National Science Foundation OCE-1834208 (YR)

608 **Author contributions:**

609 Conceptualization: PUC, JDS  
610 Methodology: JDS, YR, DP, SWH, PUC, PJB, NGP  
611 Investigation: PUC, JDS, YR, DP, SWH, PK, PJB  
612 Writing – original draft: PUC  
613 Writing – review & editing: PUC, JDS, YR, DP, SWH, PK, PJB, JMG, DPS, CZ, ZL, NGP

614 **Competing interests:** Authors declare that they have no competing interests.

615 **Data Availability Statement:** All data are available in the supplementary materials.

616

617 **Supplementary Materials**

618 Materials and Methods  
619 Figs. S1 to S10  
620 Table S1  
621 References (XX-XX)

622

623



649 **1. Assessment of GMSL reconstructions**

650 Two different approaches have been used to decompose the  $\delta^{18}\text{O}$  record measured in  
651 benthic foraminifera ( $\delta^{18}\text{O}_b$ ) into its two primary components: the temperature ( $\delta^{18}\text{O}_T$ ) and the  
652  $\delta^{18}\text{O}$  of seawater ( $\delta^{18}\text{O}_{\text{sw}}$ ) that the benthic foraminifera shells formed in, with the latter largely  
653 reflecting sea level. Ref. (1) developed an approach that regresses independently known sea-level  
654 data (e.g., from corals) on  $\delta^{18}\text{O}_b$  for the last glacial cycle and then uses this regression to reconstruct  
655 sea level from  $\delta^{18}\text{O}_b$  records for the last four glacial cycles. Sea level is then converted to  $\delta^{18}\text{O}_{\text{sw}}$   
656 using a constant relation of  $\Delta\delta^{18}\text{O}_{\text{sw}}:\Delta\text{GMSL}$ . Refs. (2) and (3) extended the regression over the  
657 last two glacial cycles to reconstruct sea level from  $\delta^{18}\text{O}_b$  records over the last 5 Myr (figs. S1B,  
658 S6C). Refs. (4, 5) further extended the regression over the last 800 kyr using the LR04  $\delta^{18}\text{O}_b$  stack  
659 and a stack of sea-level records from Ref. (6) (fig. S7C) to reconstruct sea level over the last 40  
660 Myr (figs. S1B and S6A show last 4.5 Myr). Refs. (4, 5) also accounted for  $\delta^{18}\text{O}$  variations in land  
661 ice ( $\delta^{18}\text{O}_i$ ) over the last glacial cycle which they then applied to their sea-level record to derive  
662  $\delta^{18}\text{O}_{\text{sw}}$  from  $\delta^{18}\text{O}_b$ , but this did not include the effect of increasing temperatures on  $\delta^{18}\text{O}_i$  prior to  
663 0.8 Ma. In any event, applying this regression approach to a  $\delta^{18}\text{O}_b$  record will, by default,  
664 reproduce the variability of the  $\delta^{18}\text{O}_b$  record, including the increase in the size of glaciations during  
665 the mid-Pleistocene transition (MPT), with the early Pleistocene low-amplitude variability further  
666 reinforced by not accounting for higher temperatures on  $\delta^{18}\text{O}_i$ .

667 Refs. (7) and (8) reconstructed sea level using a simple scaling relationship that determines  
668 the fraction of the LGM sea-level lowstand (-120 m in their case) from the fraction of the  $\delta^{18}\text{O}_b$   
669 value at any given time relative to the LGM  $\delta^{18}\text{O}_b$  value. As with the regression method, this  
670 relationship reproduces the  $\delta^{18}\text{O}_b$  variability throughout the Pleistocene as well as does not account  
671 for the effect of increasing temperatures on  $\delta^{18}\text{O}_i$  prior to 0.8 Ma, resulting in smaller early

672 Pleistocene ice sheets than in our reconstruction (figs. S1B, S6D). Finally, these approaches imply  
673 a stationary partitioning of  $\delta^{18}\text{O}_b$  between temperature and ice volume, and thus do not capture the  
674 larger ice volume component relative to temperature that we identify before the MPT (9).

675 Another approach that is similar to ours subtracts independently reconstructed seawater  
676 temperature as  $\delta^{18}\text{O}_T$  from  $\delta^{18}\text{O}_b$  to derive  $\delta^{18}\text{O}_{\text{sw}}$  (10-15) which can then be converted to GMSL  
677 using a relation of  $\Delta\delta^{18}\text{O}_{\text{sw}}:\Delta\text{GMSL}$  (10, 15). Ref. (15) used a reconstruction of bottom water  
678 temperature (BWT) that is similar to ours in showing lower  $\Delta\text{BWT}$  than  $\Delta\text{SST}$  during the early  
679 Pleistocene (9). However, this is a 2-Myr smoothed record and thus does not capture the increase  
680 in orbital variability across the MPT (9) (figs. S1B, S6B) which contributes to larger early  
681 Pleistocene ice sheets in our reconstruction. Ref. (15) also applied a constant  $0.013\text{\textperthousand m}^{-1}$   
682 relationship to derive sea level from their  $\delta^{18}\text{O}_{\text{sw}}$  which does not account for the effect of warmer  
683 early Pleistocene temperatures on  $\delta^{18}\text{O}_i$ , and thus  $\delta^{18}\text{O}_{\text{sw}}$ . Moreover, this relationship is more  
684 appropriate for warmer climates with just the Greenland and Antarctic ice sheets (16) as opposed  
685 to the  $0.008\text{\textperthousand m}^{-1}$  relationship that is more suitable for deriving sea level after 0.8 Ma.  
686 Accordingly, their sea-level lowstands are generally higher than in our reconstruction throughout  
687 the Pleistocene (figs. S6B, S7B).

688 Other studies that used independent orbital-scale temperature records to derive  $\delta^{18}\text{O}_{\text{sw}}$  from  
689  $\delta^{18}\text{O}_b$  suggest small GMSL variability in the late Pliocene that increases into the early Pleistocene  
690 and continues across the MPT (11, 17, 18). We used our method to convert  $\delta^{18}\text{O}_{\text{sw}}$  data from Refs.  
691 (11) and (18) to sea level (see section 2 of this Supplementary Materials) and find generally good  
692 agreement with our GMSL reconstruction (figs. S5, S6E). However, the temperature records in  
693 Refs. (11) and (18) are local and so may not be representative of mean ocean temperature (MOT).

694 Finally, other than Refs. (5) and (4), none of the reconstructions using either approach account for  
695 changing  $\delta^{18}\text{O}_i$  on  $\delta^{18}\text{O}_{\text{sw}}$  (4, 19).

696 Finally, Refs. (20, 21) reconstructed changes in water depth using grain size variations in  
697 uplifted marine sedimentary sequences preserved in New Zealand (fig. S1, S8), with inferred water  
698 depths being supplemented by estimates from benthic foraminifera. Unconformities in the  
699 sedimentary sequence are assigned a maximum water depth of -32.5 m, and the authors assume  
700 the missing part of the sea-level record to be <5 m. Water depth is converted to relative sea level  
701 using back stripping methods that account for sediment compaction and tectonic subsidence. Their  
702 reconstruction cannot be referenced to Holocene sea level, but it does identify long-term trends as  
703 well as the frequency and amplitude of sea-level change on orbital timescales. Comparison of their  
704 reconstruction to other sea-level reconstructions (fig. S1) and to our reconstruction (fig. S8) shows  
705 a similar concentration of 41-kyr variance but disagrees with these other reconstructions in  
706 showing no trend of increasing lowstands (i.e., greater amplitude) during the intensification of  
707 Northern Hemisphere glaciation.

708 **2. Conversion of  $\delta^{18}\text{O}_{\text{sw}}$  to sea level**

709 We develop a simple model to translate  $\delta^{18}\text{O}_{\text{sw}}$  to sea level that conserves global water and  
710  $^{18}\text{O}$  mass as they are redistributed between the ocean and the North American (NAIS) (Laurentide  
711 and Cordilleran ice sheets), Eurasian (EUR), Greenland (GRN), and Antarctic (ANT) ice sheets.  
712 The model also accounts for the changing isotopic composition of each ice sheet through time as  
713 a function of changes in its volume and global temperature, which allows us to separate their  
714 isotopic effects. This is important because our reconstructions suggest that there is not a constant  
715 scaling between global temperature and ice volume over the past 4.5 Myr.

716 The method is based on conservation of global water and isotopic  $^{18}\text{O}$  mass, extending  
717 similar treatments in Ref. (16) and Ref. (22). A simple expression is used for the mean  $\delta^{18}\text{O}$  of  
718 each ice sheet as a linearized function of its size and global mean surface temperature (GMST),  
719 and a parameterization is assumed for the relative size of each ice sheet to the others at all times.  
720 After some tedious but straightforward algebra, this yields a quadratic equation yielding total ice  
721 volume over flotation (and hence global sea-level rise) as a function of  $\delta^{18}\text{O}_{\text{sw}}$  and GMST.

722 While  $\delta^{18}\text{O}_{\text{sw}}$  is often converted to sea level using a constant scaling of  $\sim 0.008\text{‰}/\text{m}$  based  
723 on Last Glacial Maximum values (i.e., a  $\sim 1\text{‰}$   $\delta^{18}\text{O}_{\text{sw}}$  enrichment (23) and  $\sim 130\text{ m}$  sea level  
724 lowering (24)), our model accounts for time-varying temperature and ice-volume effects on ice-  
725 sheet  $\delta^{18}\text{O}_i$  (fig. S3D), yielding a variable relationship between  $\delta^{18}\text{O}_{\text{sw}}$  and sea level (fig. S3A,  
726 S3B). As a result, relative to linear scaling, applying our model to our  $\delta^{18}\text{O}_{\text{sw}}$  reconstruction  
727 produces lower sea levels during early Pleistocene glaciations because less-negative  $\delta^{18}\text{O}_{\text{ice}}$  then  
728 (due to higher temperatures) requires greater ice growth to explain  $\delta^{18}\text{O}_{\text{sw}}$  enrichments, and thus  
729 lower sea levels during Pliocene interglaciations because more-negative  $\delta^{18}\text{O}_{\text{ice}}$  then (due to NAIS  
730 and EIS absence) requires less ice loss to explain  $\delta^{18}\text{O}_{\text{sw}}$  depletions (fig. S3A).

731 In the remainder of this section, we explain the details of our model. Section 2.1 derives  
732 separate equations for differing climates relative to today. Section 2.2 outlines how we estimate  
733 the coefficients in the expression for mean ice-sheet  $\delta^{18}\text{O}$  based on observed quantities and  
734 published general circulation model (GCM) experiments. Section 2.3 explains the scheme we use  
735 to account for the residence time of ice in each ice sheet, and a list of prescribed quantities is given  
736 in section 2.4. Finally, section 2.5 assesses the sensitivity of our sea-level reconstruction to the  
737 various parameters in our model.

738 **2.1. Equations for differing climates**

739 Separate derivations are needed for (a) generally colder time intervals when all four ice  
740 sheets exist and sea level is below present (section 2.1.1), (b) generally warmer intervals when  
741 ANT and GRN exist with sea level 0 to 14 m above present (section 2.1.2), and (c) much warmer  
742 intervals when GRN is completely melted and only ANT exists with sea level > 14 m above present  
743 (section 2.1.3). For a given pair of  $\delta^{18}\text{O}_{\text{sw}}$  and GMST values, we cannot tell *a priori* which of the  
744 three derivations (sections 2.1.1 to 2.1.3) is appropriate. For every pair of these values in our data  
745 (with time stepping from 4.5 to 0 Ma), the quadratic solutions to the unknown K (equation 10) of  
746 all three derivations were tested, always finding at most one valid real solution with computed sea  
747 level within the required range for that derivation.

748 The subscript  $i$  is used below for each ice sheet ( $i = 1$  to 4), and summation over them is  
749 indicated by  $\Sigma[\dots]$ .

750 *2.1.1. Equations for generally colder climates (NAIS, EUR, GRN, ANT all larger than present; sea  
751 level < 0 m)*

752 Starting with the conservation equations for global water and  $^{18}\text{O}$  mass

$$V_{\text{om}} + \Sigma[V_{\text{im}}] = V_o + \Sigma[V_i] \quad (1)$$

$$V_{\text{om}} \delta_{\text{om}} + \Sigma[V_{\text{im}} \delta_{\text{im}}] = V_o \delta_o + \Sigma[V_i \delta_i] \quad (2)$$

755 where

756  $V_o$  = ocean volume,

757  $\delta_o$  = ocean water  $\delta^{18}\text{O}$ , or  $\delta^{18}\text{O}_{\text{sw}}$

758  $V_i$  = volume of each ice sheet (liquid equivalent),

759  $\delta_i$  = mean  $\delta^{18}\text{O}$  of each ice sheet, or  $\delta^{18}\text{O}_i$

760  $V_{\text{om}}$ ,  $\delta_{\text{om}}$ ,  $V_{\text{im}}$ ,  $\delta_{\text{im}}$  are the modern values of these quantities ( $V_{\text{im}} = 0$  for NAIS and EUR).

761 Eliminating  $V_o$  and rearranging,

762  $V_{om} (\delta_{om} - \delta_o) = - \sum [V_{im} (\delta_{im} - \delta_o)] + \sum [V_i (\delta_i - \delta_o)] \quad (3)$

763 We use a simple expression for the mean  $\delta^{18}\text{O}$  of each ice sheet  $i$ , linearized about the  
764 modern state for ANT and GRN, or about the nascent (first-formed) ice caps for NAIS and EUR:

765  $\delta_i = \alpha_i + \beta_i \Delta T - \gamma_i (V_i - V_{im}) \quad (4)$

766 where  $\alpha_i$  is the modern or nascent ice sheet  $\delta^{18}\text{O}$ ,  $\Delta T$  is the change in GMST from modern,  $\beta_i$  is  
767 the sensitivity to GMST with no change in volume, and  $\gamma_i$  is the sensitivity to ice-sheet volume  
768 with no change in GMST. Our estimates for the coefficients  $\alpha_i$ ,  $\beta_i$  and  $\gamma_i$  are given below in section  
769 2.2.

770 Using (4) to eliminate  $\delta_i$  in (3),

771  $V_{om} (\delta_{om} - \delta_o) = - \sum [V_{im} (\delta_{im} - \delta_o)] + \sum [V_i (\alpha_i + \beta_i \Delta T - \gamma_i (V_i - V_{im}) - \delta_o)] \quad (5)$

772 We need to solve (5) for  $V_i$  (all other terms are known). However, there are four unknowns  
773 ( $V_1$ ,  $V_2$ ,  $V_3$ ,  $V_4$ ) and only one equation, so three more equations are needed. For that, we assume  
774 that the proportional increase from modern towards LGM size is always the same for each ice  
775 sheet  $i$ , i.e.,

776  $(V_i - V_{im}) / (V_{il} - V_{im}) = K \quad (6)$

777 where  $V_{il}$  is the volume (liquid equivalent) of ice sheet  $i$  at the LGM, and  $K$  is a single number  
778 independent of ice sheet. (This only works for  $K \geq 0$ , i.e., for colder climates in which each ice  
779 sheet is bigger than modern). Observed or reasonably well agreed upon values of  $V_{il}$  and  $V_{im}$  are  
780 available for each ice sheet (section 2.4). Eq. (6) provides three additional independent equations,  
781 which are used with (5) to solve for  $K$ . To do that, it is useful to re-arrange (6):

782  $V_i = K V_{il} + (1 - K) V_{im} \quad (7)$

783 After solving for  $K$  (see below), we can recover the total ice volume:

784  $\Sigma [V_i] = K \Sigma [V_{il}] + (1 - K) \Sigma [V_{im}] \quad (8a)$

785 and total sea-level rise (SLR):

786  $SLR \times A_o = - \sum [f_i (V_i - V_{im})] = - K \sum [f_i (V_{il} - V_{im})]$  (8b)

787 where  $A_o$  = ocean area, and  $f_i$  is a typical ratio of column [height-over-flotation:ice thickness] for  
788 the ice in question, taken to be  $\sim 1000$  m/1500 m = 2/3 for ANT marine basins, and 1 for GRN,  
789 NAIS, EUR.

790 Substituting (7) into (5) and re-arranging,

791  $V_{om} (\delta_{om} - \delta_o) = - \sum [V_{im} (\delta_{im} - \delta_o)] + K \sum [V_{il} (\alpha_i + \beta_i \Delta T + \gamma_i V_{im} - \delta_o)]$   
792  $+ (1-K) \sum [V_{im} (\alpha_i + \beta_i \Delta T + \gamma_i V_{im} - \delta_o)] - K^2 \sum [(V_{il} - V_{im})^2 \gamma_i]$   
793  $- 2 K \sum [(V_{il} - V_{im}) V_{im} \gamma_i] - \sum [(V_{im})^2 \gamma_i]$  (9)

794 This is a quadratic equation in  $K$  (with all other terms known) of the form  $A K^2 + B K + C$   
795 = 0, where (in preliminary form)

796  $A = \sum [(V_{il} - V_{im})^2 \gamma_i]$   
797  $B = - \sum [V_{il} (\alpha_i + \beta_i \Delta T + \gamma_i V_{im} - \delta_o)] + \sum [V_{im} (\alpha_i + \beta_i \Delta T + \gamma_i V_{im} - \delta_o)] + 2 \sum [(V_{il} - V_{im}) V_{im} \gamma_i]$   
798  $C = V_{om} (\delta_{om} - \delta_o) + \sum [V_{im} (\delta_{im} - \delta_o)] - \sum [V_{im} (\alpha_i + \beta_i \Delta T - \delta_o)]$

799 These simplify to the final versions for A, B, and C

800  $A = \sum [(V_{il} - V_{im})^2 \gamma_i]$   
801  $B = - \sum [(V_{il} - V_{im}) (\alpha_i + \beta_i \Delta T - V_{im} \gamma_i - \delta_o)]$   
802  $C = V_{om} (\delta_{om} - \delta_o) - \sum [V_{im} \beta_i \Delta T]$

803 This final equation for C follows because  $\delta_{im} = \alpha_i$  (Eq. 4 applied to modern conditions for which  
804  $\Delta T = 0$ ).

805 The two solutions are

806  $K = (-B \pm \sqrt{B^2 - 4AC})/(2A)$  (10)

807 For colder intervals with  $\Delta T$  substantially less than 0 and  $\delta_o$  substantially greater than  $\delta_{om}$ ,  
808 it can be seen that  $A > 0$ ,  $B > 0$ ,  $C < 0$  always, so the solution with the positive square root (+ $\sqrt{}$ )  
809 will always yield positive real  $K$ , as required. Valid solutions with  $K > 0$  are also possible for  $\delta_o$   
810 very close to zero, or  $\delta_o > 0$  and  $\Delta T > 0$ . As noted above, all three quadratic solutions (in  
811 subsections 2.1.1 to 2.1.3) were tested for each combination of  $\Delta T$  and  $\delta_o$  in our data, always  
812 finding at most one valid solution with sea level in the appropriate range.

813 *2.1.2. Equations for generally warmer climates (no NAIS, EUR; smaller than present GRN, ANT;  
814 sea level 0 to 14 m above present)*

815 For moderate warming above present, there is no NAIS or EUR. ANT is present, and GRN  
816 still exists with SLR assumed to be in the range 0 to 14 m above modern. The same expression as  
817 above for mean ice-sheet  $\delta^{18}O$  is still used, but only with  $i = 1$  to 2 for ANT and GRN:

818 
$$\delta_i = \alpha_i + \beta \Delta T - \gamma_i (V_i - V_{im})$$

819 As in the derivation above for colder climates, we still have

820 
$$V_{om} (\delta_{om} - \delta_o) = - \sum [V_{im} (\delta_{im} - \delta_o)] + \sum [V_i (\alpha_i + \beta_i \Delta T - \gamma_i (V_i - V_{im}) - \delta_o)] \quad (11)$$

821 In the derivation in subsection 2.1.1, there were four unknowns ( $V_i$ ,  $i=1$  to 4), and three  
822 additional equations were needed (Eq. 6). Here there are only two unknowns ( $V_i$ ,  $i=1$  to 2), and  
823 just one additional equation is needed. We cannot use the “K” form (Eq. 6) because GRN and ANT  
824 do not decrease proportionally. Instead, we assume that both ice sheets contribute equal absolute  
825 amounts of SLR up to 14 m total, i.e.,

826 
$$(V_i - V_{im}) \text{ for GRN} = (2/3) (V_i - V_{im}) \text{ for ANT}$$

827 where 2/3 is a typical ratio of column [height-over-flootation:ice thickness] for ANT marine ice  
828 grounded below sea level. This can be written as

829 
$$\Delta V = f_i (V_i - V_{im}) \text{ for } i = 1 \text{ and } 2 \quad (12)$$

830 where  $\Delta V$  is a single number (independent of ice sheet), and  $f_i = 1$  for GRN and  $2/3$  for ANT. Of  
831 course, for consistency this requires that  $V_{2m}$  (modern Greenland) =  $7 \times A_o$ .

832 Re-writing (12) as  $V_i = \Delta V/f_i + V_{im}$  and substituting into (11) yields

$$833 V_{om} (\delta_{om} - \delta_o) = - \sum [V_{im} (\delta_{im} - \delta_o)] + \sum [(\Delta V/f_i + V_{im}) (\alpha_i + \beta_i \Delta T - \gamma_i \Delta V/f_i - \delta_o)] \quad (13)$$

834 This is a quadratic for  $\Delta V$ , of the form  $A \Delta V^2 + B \Delta V + C = 0$ .

835 Re-arranging and simplifying,

$$836 A = \sum [\gamma_i / (f_i^2)]$$

$$837 B = - \sum [(\alpha_i + \beta_i \Delta T - V_{im} \gamma_i - \delta_o) / f_i]$$

$$838 C = V_{om} (\delta_{om} - \delta_o) - \sum [V_{im} \beta_i \Delta T]$$

839 The solutions are

$$840 \Delta V = (-B \pm \sqrt{B^2 - 4AC}) / (2A) \quad (14)$$

841  $A$  is always  $< 0$ , but the signs of  $B$  and  $C$  are not readily apparent, and we cannot say *a*  
842 *priori* which sign of the square root (if any) yields a negative real  $\Delta V$  with  $-7 < \Delta V < 0$  so that  $0$   
843  $< SLR < 14$  as required. But if one exists, it is the valid solution for this interval with both GRN  
844 and ANT present.

845 Then  $V_i = \Delta V/f_i + V_{im}$ , and

$$846 SLR \times A_o = -\sum [f_i (V_i - V_{im})] = -\sum [\Delta V] = -2 \Delta V$$

#### 847 2.1.3. Equations for much warmer climates (no NAIS, EUR, GRN; sea level $> 14$ m)

848 For greater warming with GRN entirely melted, SLR is assumed to be  $> 14$  m, with only a  
849 reduced ANT existing. We still need to use equations for  $i = 1$  to 2 involving both GRN and ANT,  
850 because 7 m of the  $> 14$  m SLR is from the melted GRN. Starting with Eq. (11), the one additional  
851 equation is simply

852  $V_2 = 0$  (choosing  $i=1$  for Antarctica,  $i=2$  for Greenland).

853        Then (11) becomes an equation for Antarctic volume  $V_1$ :

854         $V_{om} (\delta_{om} - \delta_o) = - \Sigma [V_{im} (\delta_{im} - \delta_o)] + V_1 (\alpha_1 + \beta_1 \Delta T - \gamma_1 (V_1 - V_{1m}) - \delta_o)]$         (15)

855        Again, this is a quadratic for  $V_1$  of the form  $A V_1^2 + B V_1 + C = 0$ , where

856         $A = \gamma_1$

857         $B = -(\alpha_1 + \beta_1 \Delta T + \gamma_1 V_{1m} - \delta_o)$

858         $C = V_{om} (\delta_{om} - \delta_o) + \Sigma [V_{im} (\delta_{im} - \delta_o)]$

859        The two solutions are

860         $V_1 = (-B \pm \sqrt{B^2 - 4AC})/(2A)$         (16)

861        Always  $A < 0$  and  $B > 0$ , but the sign of  $C$  is not apparent, so real solutions may be possible

862        with either sign of the square root. If one is, and it is in the required range  $0 < V_1 < V_{1m} - 7 A_o /$

863         $(2/3)$  so that SLR is  $> 14$  m, then it is the valid solution for this interval with only ANT remaining,

864        and

865         $SLR \times A_o = -\Sigma [f_i (V_i - V_{im})] = V_{2m} - (2/3) (V_1 - V_{1m})$

866        For SLR up to approximately +25 m, the ANT contribution is nearly all from marine basins.

867        Using  $f_1 = 2/3$  as above is thus appropriate, and we do not need to consider ice loss from the

868        terrestrial East AIS.

869        For a very few of the combinations of mean ocean water  $\delta^{18}O_{sw}$  and global surface

870        temperature in our data (32 out of 4883), no valid quadratic solutions were found with any of the

871        three derivations described in subsections 2.1.1 to 2.1.3 above. These all occur in the Pliocene, and

872        the neighboring timesteps in the data all yield SLR close to +14 m. This is probably because the

873        physical assumptions at the border of our two “warmer” scenarios in sections 5.2 and 5.3 are too

874        restrictive, i.e., Greenland vanishing precisely at SLR = 14 m with exactly the same SLR

875 contribution as Antarctica at that point. We suspect that if these assumptions were loosened  
876 slightly, these 32 combinations would yield valid solutions with SLR close to +14 m.

877 **2.2. Estimating  $\alpha_i$ ,  $\beta_i$ , and  $\gamma_i$  values**

878 In all colder and warmer climate cases, we use a simple expression for mean ice sheet  $\delta^{18}\text{O}_i$   
879 ( $\delta_i$ ), linearized about the modern state for ANT and GRN, or about the nascent (first-formed) ice  
880 caps for NAIS and EUR ( $\alpha_i$ ):

881 
$$\delta_i = \alpha_i + \beta_i \Delta T - \gamma_i (V_i - V_{im})$$

882  $\beta_i$  describes how  $\delta_i$  responds to changes in global temperature at fixed ice-sheet size (via changes  
883 in  $\delta^{18}\text{O}$  of precipitation,  $\delta^{18}\text{O}_{\text{precip}}$ , i.e., a Dansgaard-like coefficient), and  $\gamma_i$  describes how  $\delta_i$   
884 responds to changes in ice-sheet size at fixed global temperature. The values of the coefficients  $\alpha_i$ ,  
885  $\beta_i$  and  $\gamma_i$  are obtained mostly from results of published GCM and ice-sheet model experiments (22,  
886 25-27), as described below.

887 For GRN and ANT,  $\alpha_i$  is the modern ice-sheet mean  $\delta^{18}\text{O}$ , i.e.,  $\alpha_i = \delta_{im}$ .

888 
$$\alpha_{GRN} = -34 \text{ ‰} (25)$$

889 For ANT, we combine values for the West and East Antarctic ice sheets (25), weighted by  
890 their modern volumes:

891 
$$V_{im} \text{ of WAIS} = 5 \text{ m (sea-level equivalent)} (25)$$

892 
$$\delta_{im} \text{ of WAIS} = -41 \text{ ‰} (25)$$

893 
$$V_{im} \text{ of EAIS} = 47.5 \text{ m (sea-level equivalent)} (25)$$

894 
$$\delta_{im} \text{ of EAIS} = -56.5 \text{ ‰} (25)$$

895 
$$\alpha_{ANT} = (5 * (-41) + 47.5 * (-56.5)) / (5 + 47.5) = -55 \text{ ‰}$$

896 For NAIS and EUR,  $\alpha_i$  is the  $\delta^{18}\text{O}_{\text{precip}}$  of the nascent (first-formed) ice cap for each ice  
897 sheet. We use values tuned to fit the 130 m sea-level lowstand at the LGM.

898  $A_{NAIS} = -14 \text{‰}$

899  $\alpha_{EUR}$  assumed same as NAIS = -14 ‰

900  $\beta_i$  coefficients are estimated from GCM experiments in (27) where the ice-sheet size is  
901 fixed (at modern, or with the virtual extent fixed for NAIS, EUR) and climate is changed (labelled  
902 PI and  $SST_{(LGM)}$  in (27)). The change in mean  $\delta^{18}\text{O}_{\text{precip}}$  in these experiments is assumed equal to  
903 the change in  $\delta_i$  that would result after the ice has infinite time to advect internally and equilibrate  
904 to the permanent change in climate.  $\beta_i$  is thus estimated from such GCM experiments as:

905  $\beta_i = \Delta\delta^{18}\text{O}_{\text{precip}} / \Delta T$

906 The fixed ice size in these experiments is of course artificial; an actual ice sheet would grow or  
907 retreat due to the change in surface mass balance, but this is purposely excluded in estimating  $\beta_i$ .

908 *Case 1:  $\beta_i$  and  $\gamma_i$  for colder climates than present:*

909 Using results of the  $SST_{(LGM)}$  experiment vs. modern (with fixed ice) from *Tharammal et*  
910 *al.* (27):

911  $B_{NAIS} = -1.5 \text{‰} / -2.79 \text{ °C} = 0.54 \text{‰/°C}$

912  $\beta_{EUR} = -2.77 \text{‰} / -2.79 \text{ °C} = 1 \text{‰/°C}$

913  $\beta_{GRN} = -2.6 \text{‰} / -2.79 \text{ °C} = 0.93 \text{‰/°C}$

914  $\beta_{ANT} = -1.24 \text{‰} / -2.79 \text{ °C} = 0.44 \text{‰/°C}$

915  $\gamma_i$  is the coefficient describing how  $\delta_i$  responds to changes in ice-sheet size at fixed global  
916 temperature. It is estimated using modeled changes in  $\delta_i$  for LGM vs. modern, after subtracting the  
917 component of  $\delta_i$  change due to temperature (i.e.,  $\beta_i \Delta T$ ). Subtracting the  $\delta_i$  equations for modern  
918 and LGM:

919  $\gamma_i = -[(\delta_{il} - \delta_{im}) - \beta_i \Delta T_{lgm}] / (V_{il} - V_{im})$

920 For NAIS,  $\delta_{il} - \delta_{im} = -7 \text{‰}$  (26)

921 For EUR, assume  $\delta_{il} - \delta_{im}$  = NAIS value = -7 ‰

922 For GRN,  $\delta_{il} - \delta_{im}$  = -3 ‰ (25)

923 For ANT,  $\delta_{im}$  = -55 ‰ (as calculated above from (25))

924 For ANT  $\delta_{il}$ , we combine separate values for West and East Antarctic ice sheets (WAIS, EAIS,  
925 respectively) for the LGM, from (25):

926  $V_{il}$  of WAIS = 24.6 m (sea-level equivalent)

927  $\delta_{il}$  of WAIS = -42.5 ‰ (25)

928  $V_{il}$  of EAIS = 52 m (sea-level equivalent)

929  $\delta_{il}$  of EAIS = -56.5 ‰ (25)

930  $\delta_{il} = (24.6 \times (-42.5) + 52 \times (-56.5)) / (24.6 + 52) = -52$  ‰, so

931  $\delta_{il} - \delta_{im} = +3$  ‰

932  $\Delta T_1 = -6$  °C (LGM global temperature anomaly from (28)), so:

933  $\gamma_{NAIS} = -[ -7 - 0.54 \times (-6) ] / (88 \times A_o) = 1.181 \times 10^{-16}$  ‰/m<sup>3</sup>

934  $\gamma_{EUR} = -[ -7 - 1.0 \times (-6) ] / (24.5 \times A_o) = 1.13 \times 10^{-16}$  ‰/m<sup>3</sup>

935  $\gamma_{GRN} = -[ -3 - 0.93 \times (-6) ] / (3.1 \times A_o) = -2.30 \times 10^{-15}$  ‰/m<sup>3</sup>

936  $\gamma_{ANT} = -[ +3 - 0.44 \times (-6) ] / (21.6 \times A_o) = -7.23 \times 10^{-16}$  ‰/m<sup>3</sup>

937 For NAIS and EUR,  $\gamma_i$  is positive, reflecting the lighter  $\delta^{18}\text{O}_{\text{precip}}$  on the higher ice sheet  
938 plateaus at maximum LGM size, compared to on the lower initial nascent ice patches. For GRN  
939 and ANT,  $\gamma_i$  is negative, because ice sheet expansion from modern mainly involves additional  
940 marginal marine ice growth at low elevations with heavier  $\delta^{18}\text{O}$ , compared to the existing interior  
941 ice with lighter  $\delta^{18}\text{O}$ .

942 *Case 2:  $\beta_i$  and  $\gamma_i$  for warmer climates than present (ANT and GRN only):*

943 For ANT, we assume that  $\beta_i$  estimated from (27) above for colder climates still holds for  
944 warmer climates. It measures how  $\delta^{18}\text{O}_{\text{precip}}$  changes at fixed ice-sheet size, and presumably that  
945 is similar for positive and negative  $\Delta T$ .

946 So,  $\beta_{\text{ANT}} = 0.44 \text{‰}/^{\circ}\text{C}$

947 For  $\gamma_{\text{ANT}}$ , similarly to above, subtracting the  $\delta_i$  equations for the modern (m) and Pliocene  
948 (p):

$$949 \gamma_i = -[(\delta_{ip} - \delta_{im}) - \beta_i (\Delta T_p)] / (V_{ip} - V_{im})$$

950 From Table 1 in (22), referencing the simulation of (29),  $\beta_i \Delta T_p = 7.5 \text{‰}$ ,  $\delta_{ip} - \delta_{im} = 3.8 \text{‰}$ ,  
951 and  $V_{ip} - V_{im} = -11.3 \text{ m}$  sea-level equivalent, so that

$$952 \gamma_{\text{ANT}} = -[3.8 - 7.5] / (-11.3 \times A_o) = -9.05 \times 10^{-16} \text{‰}/\text{m}^3$$

953 This agrees quite closely with  $\gamma_{\text{ANT}}$  derived above for colder climates; both are negative,  
954 representing changes in low-elevation marine ice with  $\delta^{18}\text{O} \sim -40 \text{‰}$ , while terrestrial (mostly  
955 EAIS) ice remains ~constant with  $\delta^{18}\text{O} \sim -55 \text{‰}$ . This is valid for warmer climates only up to SLR  
956  $\sim + 25 \text{ m}$ , when essentially all ANT marine basins have retreated. Beyond that, EAIS terrestrial  
957 ice would retreat back to the nascent point, and  $\gamma_i$  would be positive, but this situation is not  
958 applicable to the past 4.5 Myr.

959 For GRN, we use the same  $\beta_i = 0.93$  as for colder climates above, but a different  $\gamma_i$ , because  
960 unlike Antarctica, retreat from modern is mostly into terrestrial ice, not marine. Since no retreated-  
961 Greenland isotopic model simulations are available to our knowledge, we assume the same  $\gamma_i$  as  
962 for EUR in cold climates above:

$$963 \gamma_{\text{GRN}} = 1.35 \times 10^{-16} \text{‰}/\text{m}^3$$

964 **2.3. Time averaging  $\Delta T$  based on ice residence time**

965        The  $\beta_i \Delta T$  term in the equation for  $\delta_i$  above is for equilibrated changes, i.e., after the ice  
966        has infinite time to respond to a permanent change in climate and  $\delta^{18}\text{O}_{\text{precip}}$ . However, in a real ice  
967        sheet  $\Delta\delta^{18}\text{O}_i$  records  $\Delta\delta^{18}\text{O}_{\text{precip}}$  over a past interval on the order of the mean residence time of ice  
968        within the ice sheet. To crudely account for this, the  $\delta_i$  equation for the time-evolving ice sheets is  
969        modified to:

970        
$$\delta_i = \alpha_i + \beta_i \text{INT}[\Delta T] - \gamma_i (V_i - V_{i\text{m}})$$

971        where  $\text{INT}[\Delta T]$  is the time average of  $\Delta T$  from  $t-\tau'$  to  $t$ ,  $t$  is the current time, and  $\tau'$  is the minimum  
972        of the average ice age ( $\tau_i$ ) and how long ago the ice sheet last vanished ( $V_i = 0$ ), because if the ice  
973        sheet vanishes, its ice- $\delta^{18}\text{O}$  memory is wiped out. Then all occurrences of  $\Delta T$  are replaced by  
974         $\text{INT}[\Delta T]$  in Eqs. (5), (9), and the equations for the quadratic coefficients B and C in all cases  
975        above.

976        For GRN and ANT, mean residence times are obtained directly from (25), averaging their  
977        West and East Antarctic values together for ANT in the ratio 5:50:

978        
$$\tau_{\text{ANT}} = (5 \times 44 + 50 \times 125)/55 = 118 \text{ kyr}$$

979        
$$\tau_{\text{GRN}} = 41 \text{ kyr}$$

980        For NAIS, we assume that the average residence time is on the order of one glacial cycle:  
981        
$$\tau_{\text{NAIS}} = 100 \text{ kyr}$$

982        For EIS, it is assumed to be roughly midway between GRN and NAIS:

983        
$$\tau_{\text{EIS}} = 60 \text{ kyr}$$

984        We note that  $\tau = 41$  kyr should be used for the 41-kyr world (pre-MPT), but this issue is  
985        partially accounted for by using  $\tau'$  as the minimum of the nominal value and the interval from the  
986        last time the ice sheet vanished ( $V_i = 0$ ) to the current time.  $\tau'$  thus will not be longer than 41 kyr

987 if  $V_i(t)$  is decreasing to zero realistically as it should in the 41-kyr world. This “minimum”  
988 correction reduces the nominal  $\tau$  values for the 41-kyr world.

989 **2.4. List of prescribed quantities**

990  $V_{om}$  = modern ocean volume =  $1.35 \times 10^{18} \text{ m}^3$

991  $A_o$  = ocean area =  $3.62 \times 10^{14} \text{ m}^2$

992  $\delta_{om}$  = modern ocean  $\delta^{18}\text{O}$  = 0 ‰

993  $V_{im}$  = modern volume of ice sheet i (liquid equivalent) = sea level change x  $A_o$ :

994  $NAIS = 0 \text{ m} \times A_o = 0 \text{ m}^3$

995  $EIS = 0 \text{ m} \times A_o = 0 \text{ m}^3$

996  $GRN = 6.7 \text{ m} \times A_o = 2.47 \times 10^{15} \text{ m}^3$

997  $WAIS = 5 \text{ m} \times A_o = 1.81 \times 10^{15} \text{ m}^3$

998  $EAIS = 47.5 \text{ m} \times A_o = 1.72 \times 10^{16} \text{ m}^3$

999  $ANT = WAIS + EAIS = 52.5 \text{ m} \times A_o = 1.94 \times 10^{16} \text{ m}^3$

1000  $V_{il}$  = LGM volume of ice sheet i (liquid equivalent) = sea level equivalent x  $A_o$ :

1001  $NAIS = 88 \text{ m} \times A_o = 3.19 \times 10^{16} \text{ m}^3$  (30)

1002  $EIS = 24.5 \text{ m} \times A_o = 8.87 \times 10^{15} \text{ m}^3$  (modified from 23.5 m in (30))

1003  $GRN = 3.1 \text{ m (LGM excess)} \times A_o = 1.12 \times 10^{15} \text{ (LGM excess)} + 2.47 \times 10^{15} \text{ (modern)}$

1004  $= 3.59 \times 10^{15} \text{ m}^3$

1005  $WAIS = 19.6 \text{ m (LGM excess)} \times A_o = 7.10 \times 10^{15} \text{ m}^3$

1006  $EAIS = 2 \text{ m (LGM excess)} \times A_o = 7.24 \times 10^{14} \text{ m}^3$

1007  $ANT = WAIS + EAIS = 21.6 \text{ m (LGM excess)}, \text{ of which } 2/3 (14.4 \text{ m}) \text{ contributes to sea level}$

1008  $ANT = 7.82 \times 10^{15} \text{ m}^3 \text{ (LGM excess)} + 1.94 \times 10^{16} \text{ m}^3 \text{ (modern)} = 2.72 \times 10^{16} \text{ m}^3$

1009 Total LGM sea-level fall =  $88 + 24.5 + 3.1 + 14.4 = 130 \text{ m}$

1010  $\delta_{\text{im}} = \text{modern } \delta^{18}\text{O of ice sheet i:}$   
1011 NAIS = -14 ‰  
1012 EIS = -14 ‰  
1013 GRN = -34 ‰ (25)  
1014 WAIS = -41 ‰ (25)  
1015 EAIS = -56.5 ‰ (25)  
1016 ANT = WAIS + EAIS =  $[5x(-41) + 47.5x(-56.5)] / [5+47.5] = -55 \text{ ‰}$

1017  $\delta_{\text{il}} = \text{LGM } \delta^{18}\text{O of ice sheet i:}$   
1018 NAIS = -21 ‰  
1019 EIS = -21 ‰  
1020 GRN = -37 ‰ (25)  
1021 WAIS = -42.5 ‰ (25)  
1022 EAIS = -56.5 ‰ (25)  
1023 ANT = WAIS + EAIS =  $[24.6*(-42.5) + 52*(-56.5)] / [24.6+52] = -52 \text{ ‰}$

1024  
1025

1026 **2.5. Sea-level reconstruction sensitivity tests**

1027 The dependence of  $\delta^{18}\text{O}_{\text{ice}}$  on ice elevation and temperature may have differed further back  
1028 in time due to changes in ice-sheet geometry, temperature gradients, and accumulation seasonality.  
1029 We thus conducted several sensitivity tests to explore the robustness of our sea-level reconstruction  
1030 to these dependencies. We first altered the  $\beta_i$  values in our model by a factor of two higher and  
1031 lower, adjusting  $\alpha_i$  and  $\gamma_i$  values to be consistent with these perturbed  $\beta_i$  values and the LGM ice-  
1032 sheet volume and  $\delta^{18}\text{O}$  changes used in our standard scenario. These changes in  $\beta_i$  mostly affect

1033 the magnitude of sea-level lowstands during early Pleistocene glaciations, in particular deepening  
1034 them with larger  $\beta_i$  values because this yields heavier  $\delta^{18}\text{O}_i$  due to warmer temperatures (fig. S4A).  
1035 We next found that  $1\sigma$  uncertainties of 0.2 to 0.6°C in our  $\Delta\text{MOT}$  reconstruction used to derive  
1036  $\delta^{18}\text{O}_{\text{sw}}$  (9) translate to  $\delta^{18}\text{O}_{\text{sw}}$  uncertainties of ~0.05 to 0.15 ‰ and corresponding sea-level  
1037 uncertainties of ~5 to 25 m (fig. S4B). These uncertainties are typically larger in the late  
1038 Pleistocene due to the higher MOT:SST scaling then, as well as in the Pliocene due to the smaller  
1039 number of SST records used to derive MOT (9).

1040 Lastly, we evaluated how much an underestimation of MOT glacial-interglacial variability  
1041 prior to the MPT might affect reconstructed sea levels by recalculating sea levels after amplifying  
1042 the power in the orbital bands (15-25 and 35-45 kyr) in our  $\Delta\text{MOT}$  reconstruction (9) prior to 1  
1043 Ma by factors of five and ten. The resulting sea-level reconstructions show that sea-level lowstands  
1044 during the early Pleistocene remained below -100 m regardless of the scenario (fig. S4C).  
1045 Although these sensitivity analyses reveal how various details of our GMSL reconstruction could  
1046 be altered by future work, they suggest that our finding of LGM-like sea-level lowstands during  
1047 the early Pleistocene is robust across a wide range of parameter values in our model and is  
1048 consistent with several lines of geological evidence.

1049 **3. Time series analyses**

1050 We characterized the temporal variability and covariability of the different time series in  
1051 four ways, using: 1) evolutionary spectra (Fig. 2A); 2) “global” multitaper spectral analysis (Fig.  
1052 2B); 3) bandpass-filtered time series of  $\Delta\text{GMST}$  and SL at the 41 kyr obliquity period (Fig. 2C);  
1053 and 4) the rolling coherence between the filtered series and obliquity (Fig. 2D). Evolutionary  
1054 spectra (31) were calculated using the R astrochron package (32, 33). The function `eha()` in the  
1055 astrochron package implements a moving-window application of the multi-taper method (MTM)

1056 spectral-analysis procedure (34). We used a window width of 500 kyr, a time step of 10 kyr  
1057 between adjacent window positions, and a “standard” MTM time-bandwidth product of 4. Prior to  
1058 analysis, the time series were detrended using a smoothing spline with 10 degrees of freedom using  
1059 the `spline.smooth()` function in the R base stats package (33). This detrending step removes the  
1060 very long-period variability from the time series but does not obscure or overly emphasize the  
1061 eccentricity band variations in the data. The spectral density was rescaled to “normalized  
1062 amplitude” values—in each window, the amplitudes (the square root of the spectral density) at  
1063 each frequency were divided by the maximum amplitude across all frequencies. This facilitates  
1064 judging the relative importance of variations across periods. We did not do any significance testing  
1065 of the results because the presence of variability in the time series at orbital frequencies is really  
1066 not in question, and white-noise or low-order autoregressive null-hypothesis spectra are rather  
1067 naïve. On Fig. 2A, the dominant periods in insolation variations at orbital periods are indicated by  
1068 horizontal lines (eccentricity:  $E_1 = 400$  kyr,  $E_2 = 96$  kyr; obliquity:  $T = 41$  kyr and precession:  $P_1$   
1069  $= 23$  kyr,  $P_2 = 19$  kyr).

1070 Global (as opposed to evolutionary) spectral analysis was performed for blocks of data, as  
1071 indicated by the black horizontal bars on Fig. 2A. We used the multitaper method here as well.  
1072 We bandpass-filtered the time series at the 41 kyr obliquity period using the `butter()` (Butterworth  
1073 filter) function from the R `signal` package (35). The band limits were 39.0 and 43.1 kyr, 0.95 and  
1074 1.05 times the obliquity frequency of  $1/41.0 = 0.0244$  cycles kyr<sup>-1</sup>. The coherence between  
1075 obliquity and  $\Delta$ GMST and SL was calculated using a moving window approach. Cross-spectral  
1076 analyses were done following the Blackman-Tukey method using the `SPECTX2` function from the  
1077 ARAND software package (36). The number of lags used correspond to  $\sim 1/3$  the length of the  
1078 interval analyzed.

1079 **4. Ice-sheet surface mass balance**

1080 We assessed the sensitivity of the surface mass balance (SMB) of early Pleistocene  
1081 Northern Hemisphere ice sheets to orbits, atmospheric CO<sub>2</sub>, and ice-sheet height by conducting  
1082 experiments with the GENESIS V3.0 climate model (37, 38) (Table S1). The GENESIS climate  
1083 model comprises a T31 atmospheric model (horizontal resolution of approximately 3.75° × 3.75°  
1084 latitude by longitude) coupled with the land-surface model LSX (2° × 2° resolution). SSTs were  
1085 computed by the 50-meter mixed layer ocean model in GENESIS. SMB is computed from annual  
1086 precipitation, runoff, and evaporation over the ice sheets on the 2° × 2° grid of the LSX land surface  
1087 model. The fraction of runoff retained through refreezing is computed as a function of temperature  
1088 and precipitation using the method of Ref. (39). We ran the simulations for 100 years and analyzed  
1089 the last 70 years to exclude spin-up artifacts.

1090 Our sensitivity experiments used orbits corresponding to low (glacial) and high  
1091 (interglacial) obliquity at 2.165 Ma and 2.145 Ma (40), respectively, and atmospheric CO<sub>2</sub> values  
1092 of 200 and 300 ppmv which cover much of the early Pleistocene range suggested by proxies (41-  
1093 43). We used three ice-sheet configurations to assess sensitivity to ice-sheet height for a given  
1094 LGM area (Table S1). The GLAC-1D LGM ice sheets are from Ref. (44). The HIGH ice sheets  
1095 are intended to represent the largest of the early Pleistocene ice sheets, with ~30 m of additional  
1096 lowering of sea-level relative to the LGM sea-level lowstand (Figs. 1C, 3E). We derived the HIGH  
1097 ice-sheet heights by calculating the volume of 30 m of global sea level and distributing the height  
1098 equivalent of the volume uniformly over the GLAC 1-D LGM North American (NA) (20 m) and  
1099 Eurasian (EU) (10 m) ice-sheet complexes, accounting for the density ratio of water to ice (1028  
1100 kg m<sup>-3</sup>/910 kg m<sup>-3</sup>). The LOW ice sheet was derived by reducing the GLAC 1-D LGM ice-sheet

1101 height to an equivalent of 60% of the full LGM sea-level volume and is intended to represent the  
1102 low-aspect ratio ice-sheet geometry inferred from the regolith hypothesis (45).

1103 Experiment EXP1 shows the model's ability to simulate NH (GLAC-1D) ice sheets that  
1104 are in SMB or have positive SMB under LGM boundary conditions (Table S1). Experiments EXP2  
1105 and EXP3 assess the effect of orbital changes on NH ice-sheet SMB (Table S1). In both  
1106 experiments, NH MATs north of 40°N are 8 K to 9 K colder than the PI due to the presence of the  
1107 ice sheets while North Atlantic SSTs are 3 K to >5 K colder due to advection of cold air off the  
1108 NA ice-sheet complex and southward expansion of sea ice (fig. S10A). Warming of the oceans  
1109 elsewhere partially offsets the NH cooling such that global SSTs are the same as PI and global  
1110 MATs are 2 K colder than PI (Table S1). The net effect of the boundary conditions yields a glacial  
1111 NA ice-sheet-complex SMB of 5 m yr<sup>-1</sup> (fig. S10B) and an interglacial SMB of -11 m yr<sup>-1</sup>.  
1112 Comparison of the NA and EU ice-sheet-complex SMB in EXP2 to that of EXP3 indicates that  
1113 glacial-interglacial obliquity accounts for 16 m yr<sup>-1</sup> over NA and 2 m yr<sup>-1</sup> over EU (Table S1, fig.  
1114 S10C).

1115 Experiments EXP2 and EXP4 assess the effect of CO<sub>2</sub> changes on NH ice-sheet SMB.  
1116 Over the 200 to 300 ppm range evaluated here, CO<sub>2</sub> accounts for 15 m yr<sup>-1</sup> in the NA ice-sheet  
1117 complex SMB and 8 m yr<sup>-1</sup> in the EU ice-sheet complex SMB, which are comparable to the effect  
1118 of obliquity (Table S1). Experiments EXP2 and EXP5 and experiments EXP4 and EXP6 assess  
1119 the effect of ice-sheet height on NH ice-sheet SMB (Table S1). Lowering the ice-sheet height from  
1120 HIGH (EXP2) to GLAC-1D (EXP5) results in SMB becoming more negative by 35 m yr<sup>-1</sup> for the  
1121 NA ice-sheet complex and 11 m yr<sup>-1</sup> for the EU ice-sheet complex (Table S1). The effect of height  
1122 on mass balance is most evident along the margin of the NA ice-sheet complex (fig. S10D) where  
1123 the higher margin blocks penetration of precipitation into the interior (orographic shadowing) and

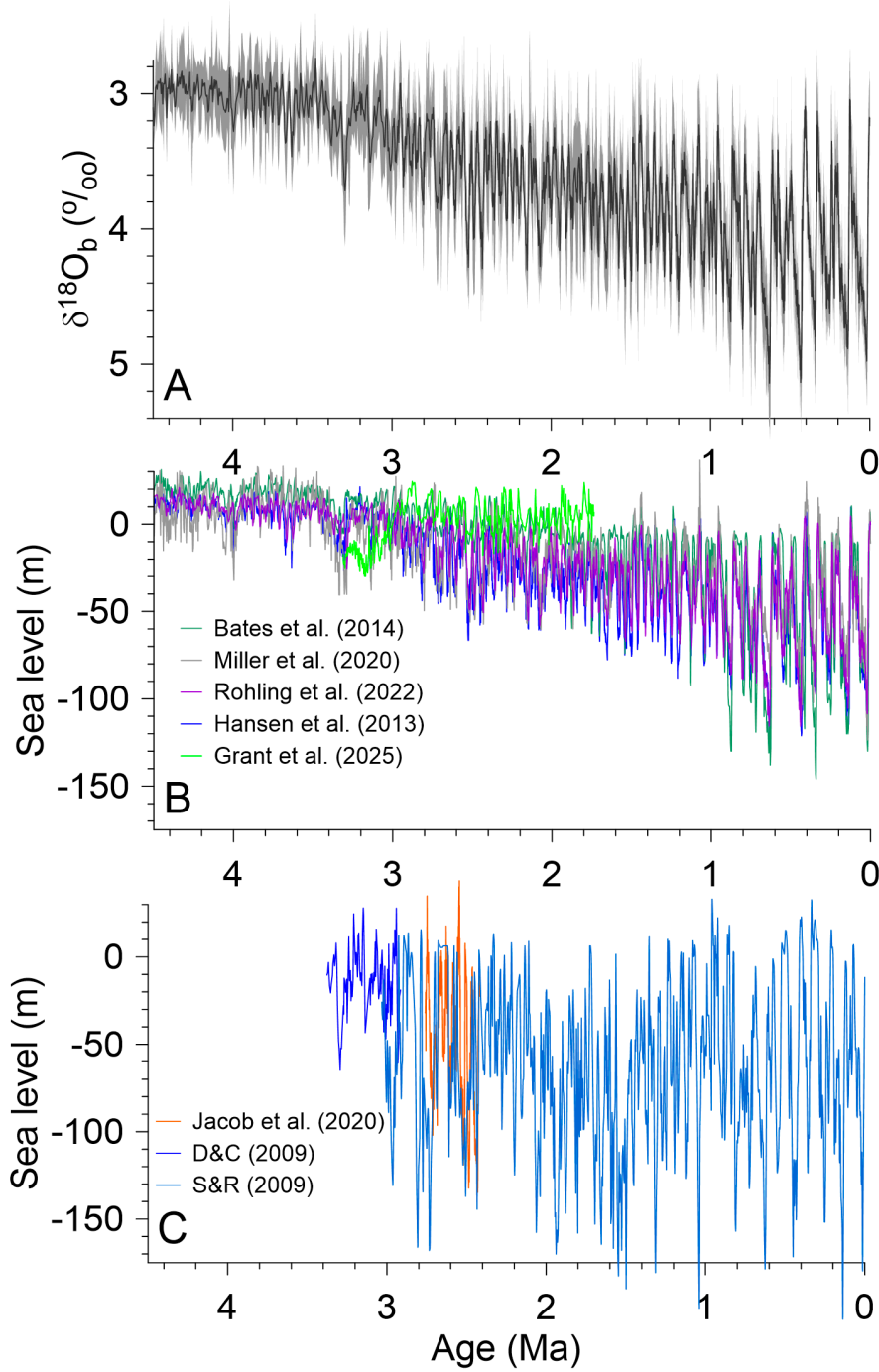
1124 positions more ice area at or above the zero-degree isotherm. The marginally more positive SMB  
1125 over the interior of the NA ice-sheet complex for the lower ice sheet where precipitation is slightly  
1126 greater than that of the high ice sheet reflects the effect of desertification.

1127 Lowering the ice sheet from HIGH (EXP4) to LOW (EXP6) results in SMB becoming  
1128 more negative by  $84 \text{ m yr}^{-1}$  for the NA ice-sheet complex and by  $4 \text{ m yr}^{-1}$  for the EU ice-sheet  
1129 complex (Table S1). We note that the strongly negative SMB of the LOW ice sheet in EXP6 (Table  
1130 S1) indicates that such an ice sheet could not have existed even under glacial orbitals and LGM  
1131 CO<sub>2</sub> levels.

1132 In summary, our sensitivity tests suggest that early Pleistocene ice sheets that were larger  
1133 than LGM ice sheets could have been in SMB with low obliquity and CO<sub>2</sub> levels of 300 ppm. SMB  
1134 becomes more negative as ice-sheet height decreases towards LGM values unless there is a  
1135 compensatory decrease in CO<sub>2</sub>, but no decrease in CO<sub>2</sub> within the range of our current  
1136 understanding of its Pleistocene variability could support the low-aspect-ratio ice sheets in SMB  
1137 inferred by the regolith hypothesis (45). We note that while our experiments using LSX and a  
1138 mixed layer ocean model are a first-order assessment of the sensitivity of ice-sheet SMB to changes  
1139 in boundary conditions, the model does not account for feedbacks such as changes in global ocean  
1140 circulation and ice-sheet dynamics that, when investigated with a full Earth System model, would  
1141 further refine our results. The challenge remains for modeling the inception and growth of the ice  
1142 sheets.

1143  
1144  
1145  
1146  
1147  
1148  
1149  
1150

1151  
1152



1153

1154

1155

1156

1157

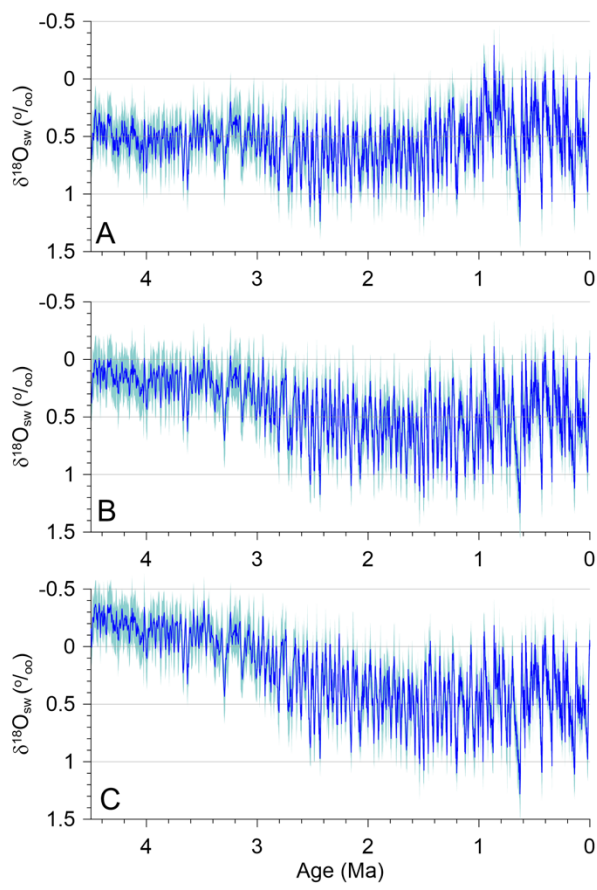
1158

1159

1160

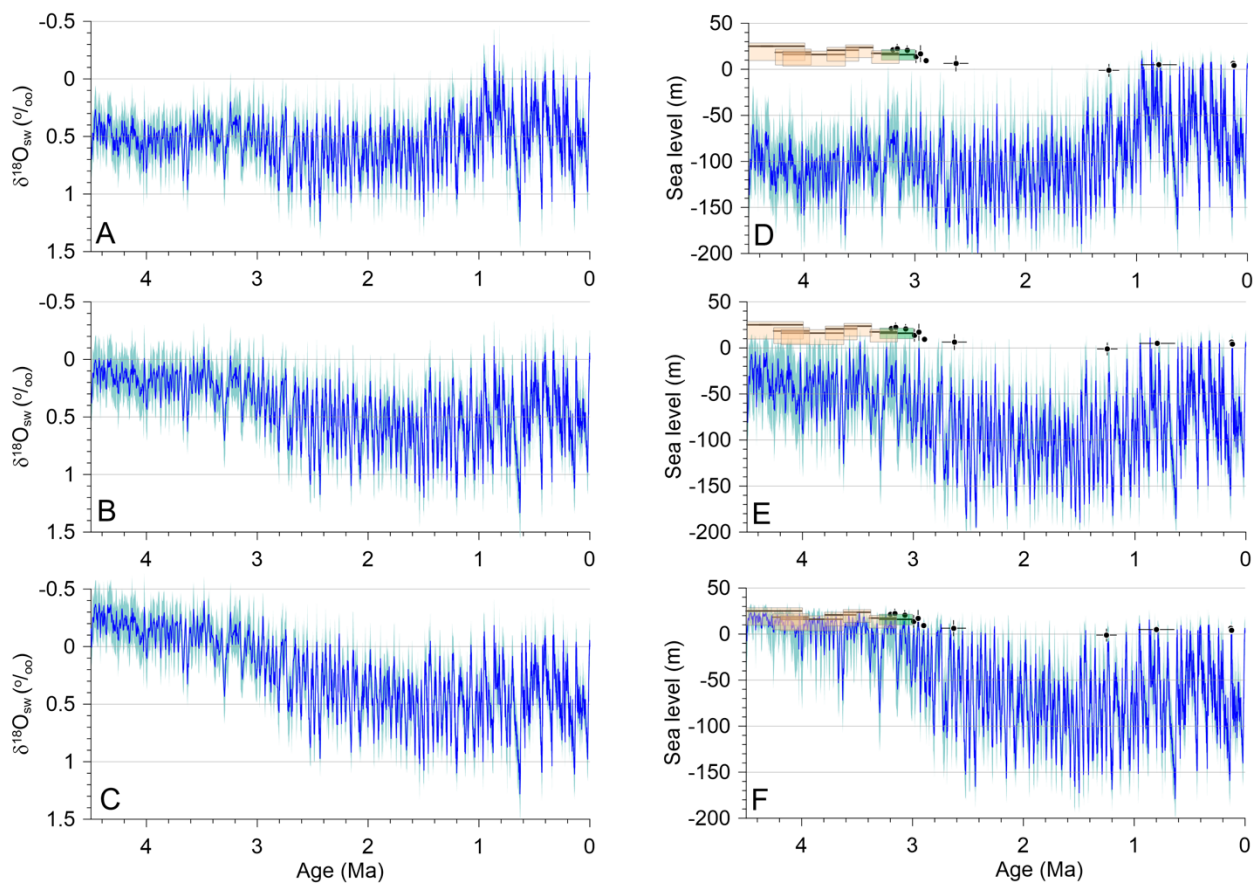
**Figure S1.** (A) Benthic  $\delta^{18}\text{O}$  stack with  $1\sigma$  uncertainty (46). (B) Reconstructions of global sea level. Blue line from Ref. (7), light green line from Ref. (3), purple line from Ref. (4), dark gray line from Ref. (15), dark green line from Refs. (20, 21). (C) Reconstructions of global sea level. Orange line from Ref. (18). Dark blue line from Ref. (17). Light blue line is based on converting the  $\delta^{18}\text{O}_{\text{sw}}$  data from Ref. (11) to sea level using our methodology.

1161



1162

Figure S2. (A) Reconstructed  $\delta^{18}\text{O}$  of seawater ( $\delta^{18}\text{O}_{\text{sw}}$ ) ( $1\sigma$  uncertainty) based on  $\Delta\text{MOT}:\Delta\text{SST} = 1$  (9). (B) Reconstructed  $\delta^{18}\text{O}_{\text{sw}}$  ( $1\sigma$  uncertainty) based on  $\Delta\text{MOT}:\Delta\text{SST} = 0.5$  before 1.5 Ma (9). (C) Reconstructed  $\delta^{18}\text{O}_{\text{sw}}$  ( $1\sigma$  uncertainty) based on  $\Delta\text{MOT}:\Delta\text{SST} = 0.5$  before 1.5 Ma and removal of long-term trend of  $0.083\text{‰ Myr}^{-1}$  (9). (D) Reconstructed sea level ( $1\sigma$  uncertainty) based on  $\delta^{18}\text{O}_{\text{sw}}$  reconstruction in (A). Also shown are published Pliocene (47-49) and Pleistocene (50, 51) sea-level highstands. (E) Reconstructed sea level ( $1\sigma$  uncertainty) based on  $\delta^{18}\text{O}_{\text{sw}}$  reconstruction in (B). Also shown are published Pliocene (47-49) and Pleistocene (50, 51) sea-level highstands. (F) Reconstructed sea level ( $1\sigma$  uncertainty) based on  $\delta^{18}\text{O}_{\text{sw}}$  reconstruction in (C), which is our final reconstruction shown in Fig. 1C. Also shown are published Pliocene (47-49) and Pleistocene (50, 51) sea-level highstands.



1163

1164

1165

1166

1167

1168

1169

1170

1171

1172

1173

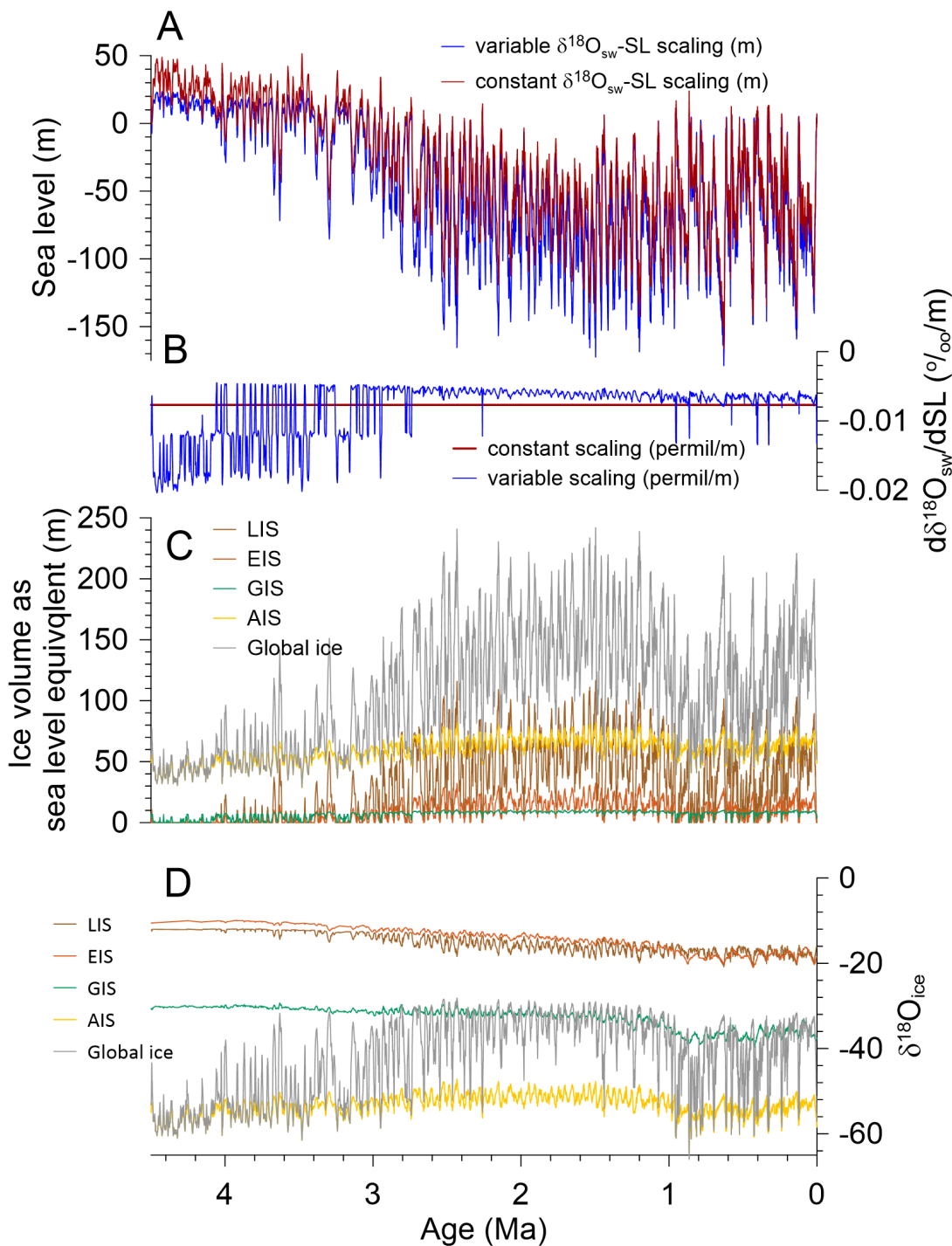
1174

1175

1176

1177

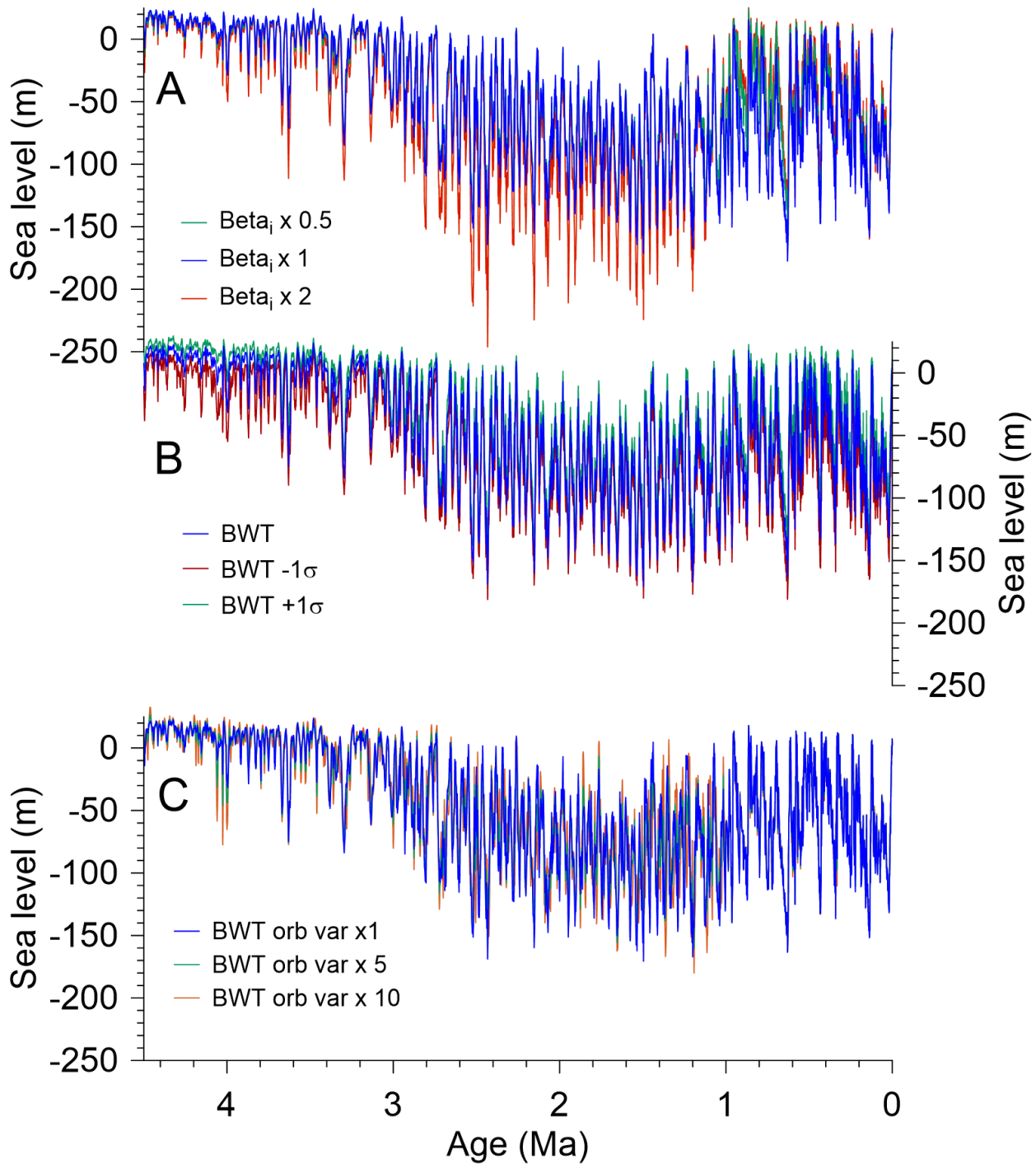
1178



1179

1180 **Figure S3.** (A) Our standard sea-level reconstruction based on variable  $\delta^{18}\text{O}_{\text{sw}}$ -sea level scaling  
 1181 (dark blue) compared to using a constant scaling of  $-0.08\text{‰ m}^{-1}$  (red). (B) The  $\delta^{18}\text{O}_{\text{sw}}$ -sea level  
 1182 scalings for the sea-level reconstructions shown in panel A. (C) Sea-level equivalent ice volumes  
 1183 from our standard reconstruction. (D) Ice-sheet mean  $\delta^{18}\text{O}$  compositions from our standard  
 1184 reconstruction.

1185  
1186  
1187



1188  
1189  
1190  
1191  
1192

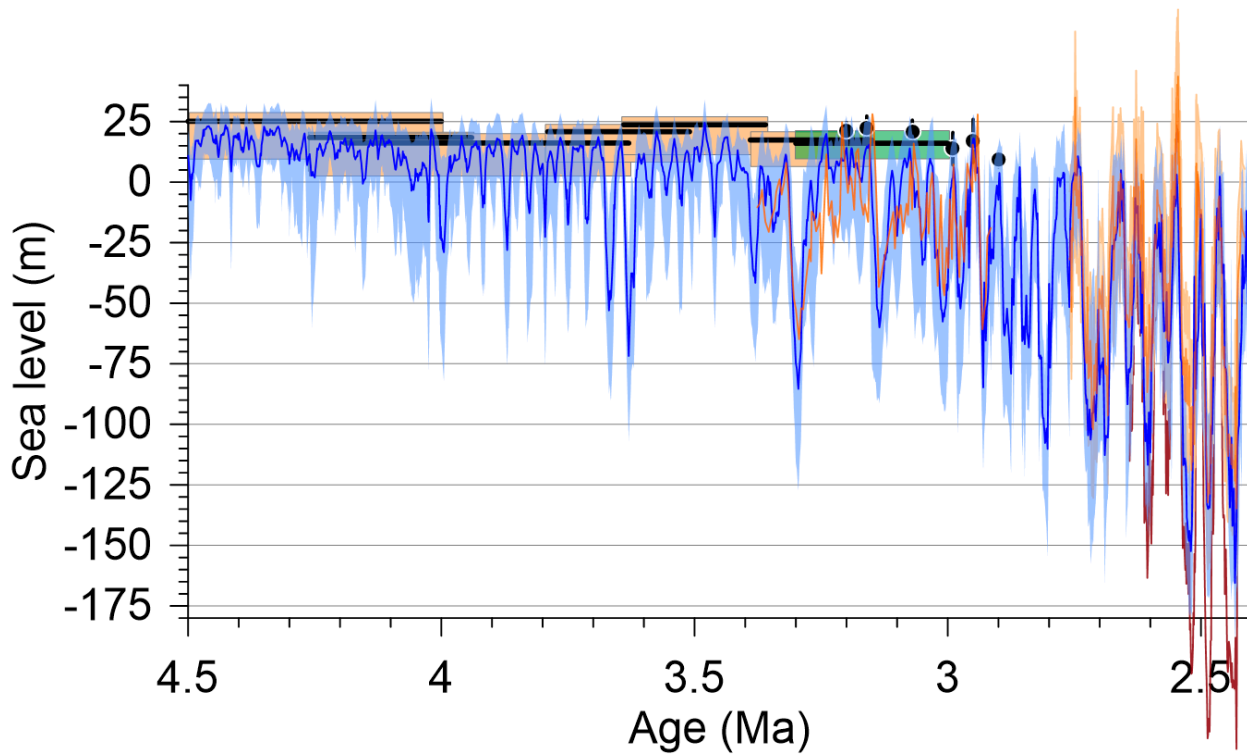
**Figure S4.** (A) Reconstructed sea level using our standard  $\beta_i$  values (blue) compared to  $\beta_i$  values that are half (green) and twice (red) as large. (B) Reconstructed sea level using our standard BWT reconstruction (blue) and its lower (red) and upper (green)  $1\sigma$  range. (C) Reconstructed sea level using our standard BWT reconstruction (blue) and reconstructions in which <100-kyr BWT

1193 variability has amplified only the power in the orbital bands (15-25 and 35-45 kyr) by a factor of  
1194 five (green) and 10 (red).

1195

1196

1197



1198

1199 **Figure S5.** Our sea-level reconstruction during the middle-to-late Pliocene (blue,  $1\sigma$  uncertainty)  
1200 compared with sea-level reconstructions from Mallorcan speleothem data (black lines = sea-level  
1201 mode and age uncertainty, height of orange boxes = 16<sup>th</sup> and 84<sup>th</sup> percentile uncertainties) (48),  
1202 Australian coral data (49), published sea-level reconstructions based on  $\delta^{18}\text{O}_{\text{sw}}$  reconstructions  
1203 from ODP site 607 (17) and site U1313 (2.4-2.75 Ma) (18) (orange lines), with our a sea-level  
1204 reconstruction for site U1313 based on our methodology, and reconstructions of sea-level high  
1205 stands from proxy data (black circles) (47).  
1206

1207

1208

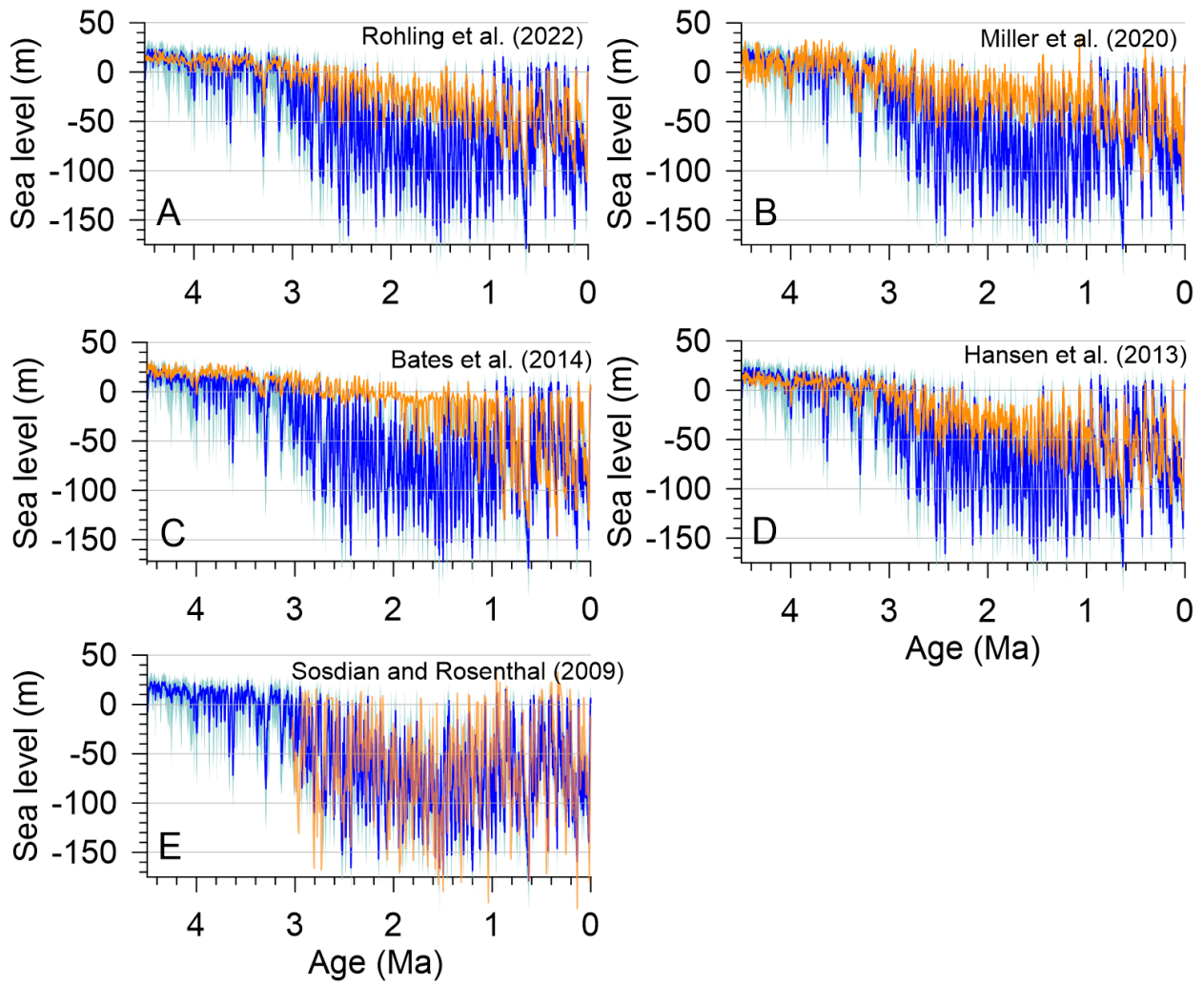
1209

1210

1211

1212

1213  
1214  
1215  
1216

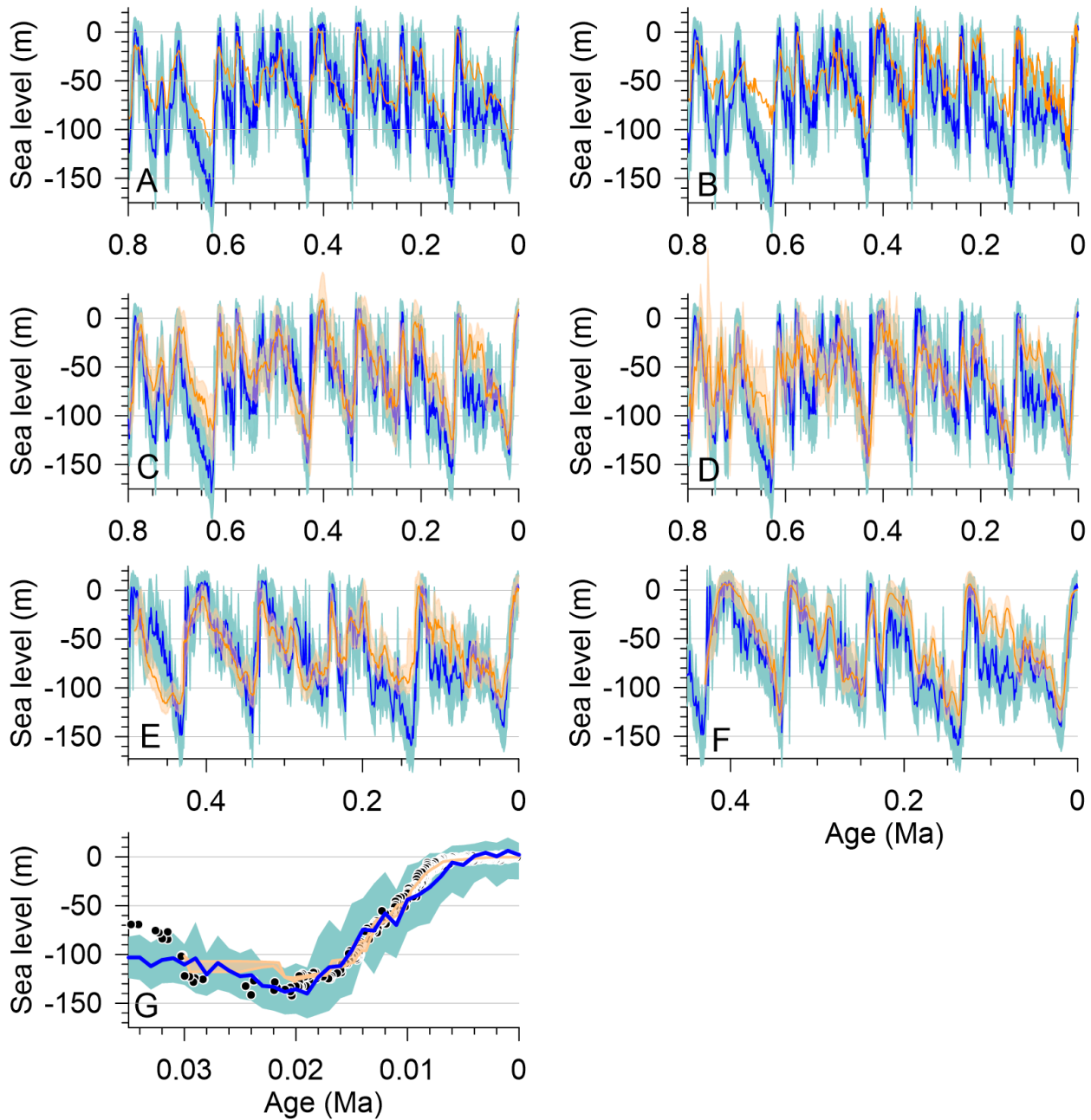


1217  
1218  
1219  
1220  
1221  
1222

**Figure S6.** Comparison of our sea-level reconstruction (blue,  $1\sigma$  uncertainty) to published reconstructions (orange) for last 4.5 Ma. (A) Sea-level reconstruction from Ref. (5). (B) Sea-level reconstruction from Ref. (15) (C) Sea-level reconstruction from Ref. (3). (D) Sea-level reconstruction from Ref. (7). (E) Sea-level reconstruction based on converting the  $\delta^{18}\text{O}_{\text{sw}}$  data from Ref. (11) to sea level using our methodology.

1223  
1224  
1225  
1226

1227  
1228  
1229  
1230



1231

1232 **Figure S7.** (Comparison of our sea-level reconstruction (blue,  $1\sigma$  uncertainty) to published  
1233 reconstructions (orange) for <0.8 Ma. (A) Sea-level reconstruction from Ref. (5). (B) Sea-level  
1234 reconstruction from Ref. (15). (C) Sea-level reconstruction from Ref. (6). (D) Sea-level  
1235 reconstruction from Ref. (10). (E) Sea-level reconstruction from Ref. (52). (F) Sea-level

1236 reconstruction from Ref. (1). (F) Sea-level reconstruction from Ref. (24) (black circles) and Ref.  
1237 (53) (orange,  $1\sigma$  uncertainty).

1238

1239

1240

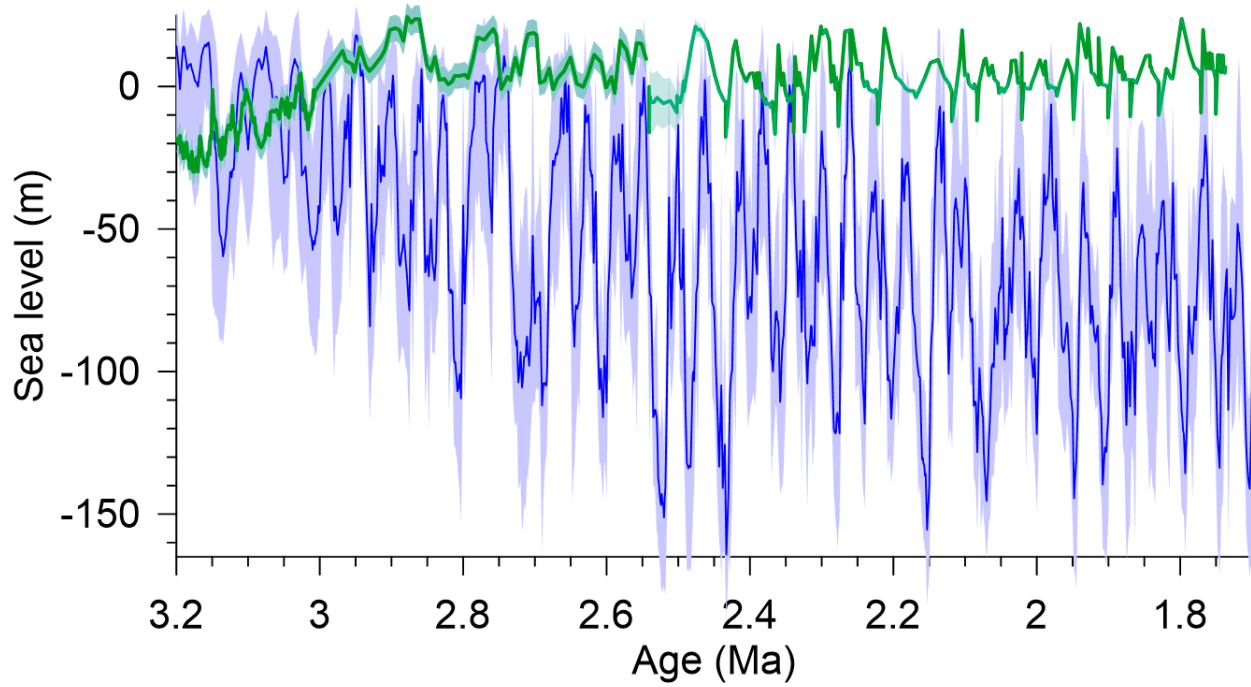
1241

1242

1243

1244

1245



1246

1247

1248 **Figure S8.** Comparison of our sea-level reconstruction (blue,  $1\sigma$  uncertainty) to reconstruction  
1249 from sediments in New Zealand (20, 21) (green) for 1.7-3.2 Ma.

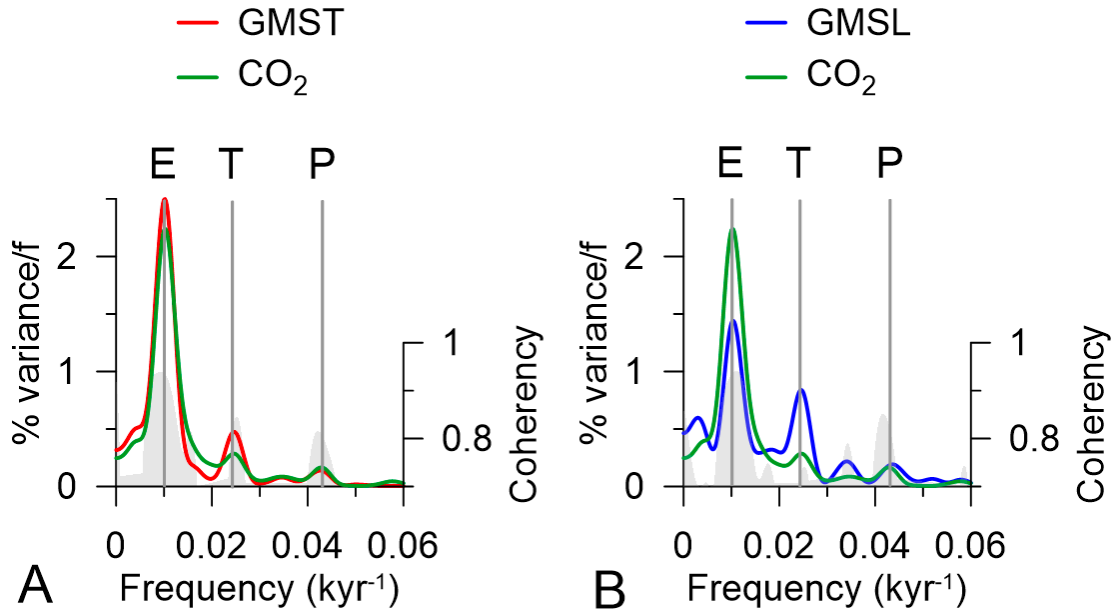
1250

1251

1252

1253

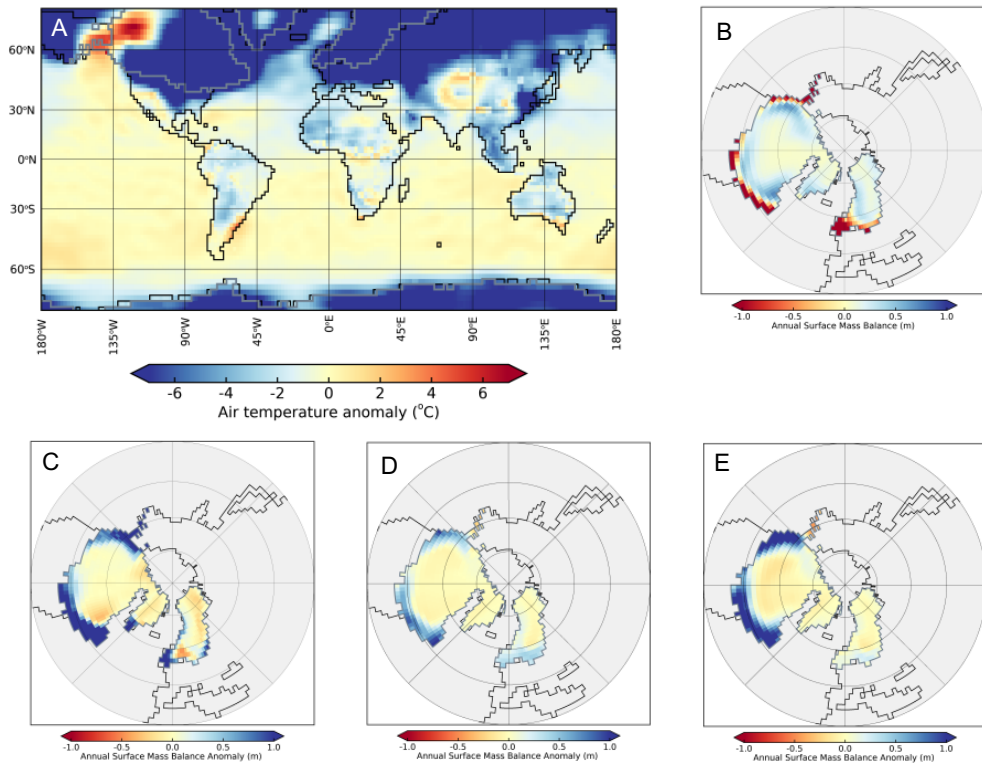
1254



1255  
1256

1257 **Figure S9.** (A) Spectral density of global mean surface temperature (GMST) and CO<sub>2</sub> and their  
1258 coherence spectra (gray shading) for the last 0.8 Myr. (B) Spectral density of global mean sea level  
1259 (GMSL) and CO<sub>2</sub> and their coherence spectra (gray shading) for the last 0.8 Myr. Frequencies of  
1260 eccentricity (E = 96 kyr), obliquity (T = 41 kyr), and precession (P = 23 kyr) shown by vertical  
1261 gray lines.

1262



1263

1264 **Figure S10.** Climate and surface mass balance simulations (Table S1). (A) EXP1 minus PI  
 1265 temperature. (B) Annual surface mass balance for EXP1. (C) EXP2 minus EXP3 annual surface  
 1266 mass balance. (D) EXP2 minus EXP5 annual surface mass balance. (E) EXP4 minus EXP6 annual  
 1267 surface mass balance. The boundary conditions for the experiments are described in Table S1.

1268

1269

1270

1271

1272

1273

1274

1275

1276

1277

1278

1279

1280

1281

1282

1283    **Table S1.** Boundary conditions, simulated mean-annual global and Northern Hemisphere  
 1284    temperatures, and ice-sheet mass balances for the North American (NA) and Eurasian (EU) ice-  
 1285    sheet complexes from sensitivity tests conducted with the GENESIS climate model using the 50-  
 1286    meter mixed layer ocean model. MAT is 2-m air temperature.

1287

Experiment	Orbitals <sup>-1</sup>	CO <sub>2</sub> (ppmV)	NH ice sheets <sup>2</sup>	Global MAT (K)	Global SST (K)	NH MAT <sup>3</sup> (K)	NH SST <sup>3</sup> (K)	NA SMB (m a <sup>-1</sup> )	EU SMB (m a <sup>-1</sup> )
PI	Present	280	Present	285	288	270	273	--	--
EXP1	LGM	200	GLAC	282	287	261	268	8	0
EXP2	Glacial	300	HIGH	283	288	262	270	5	-6
EXP3	Interglacial	300	HIGH	283	288	263	271	-11	-8
EXP4	Glacial	200	HIGH	281	286	260	268	20	2
EXP5	Glacial	300	GLAC	283	288	262	270	-30	-17
EXP6	Glacial	200	LOW	282	287	261	268	-64	-2

1288    <sup>1</sup>Glacial: 2.165 Ma; Interglacial: 2.145 Ma. Calculated from *Laskar et al.* (40).

1289    <sup>2</sup>HIGH: GLAC 1-D LGM ice height with 30 m of additional sea level distributed as 20 m over  
 1290    the LIS and 10 m over the EIS; LOW: GLAC 1-D LGM ice height reduced to 60% of the LGM  
 1291    sea level.

1292    <sup>3</sup>Poleward of 40°N.

1293

1294

1295

1296 **Data S1. (separate file)**

1297 Data\_S1.xlsx file contains global mean sea level data plotted in Fig. 1.

1298

1299 **REFERENCES AND NOTES**

- 1300 1. C. Waelbroeck *et al.*, Sea-level and deep water temperature changes derived from benthic  
1301 foraminifera isotopic records. *Quaternary Science Reviews* **21**, 295-305 (2002).
- 1302 2. M. Siddall, B. Honisch, C. Waelbroeck, P. Huybers, Changes in deep Pacific temperature  
1303 during the mid-Pleistocene transition and Quaternary. *Quaternary Science Reviews* **29**,  
1304 170-181 (2010).
- 1305 3. S. L. Bates, M. Siddall, C. Waelbroeck, Hydrographic variations in deep ocean temperature  
1306 over the mid-Pleistocene transition. *Quaternary Science Reviews* **88**, 147-158 (2014).
- 1307 4. E. J. Rohling *et al.*, Sea level and deep-sea temperature reconstructions suggest quasi-stable  
1308 states and critical transitions over the past 40 million years. *Science Advances* **7**, eabf5326  
1309 (2021).
- 1310 5. E. J. Rohling *et al.*, Comparison and synthesis of sea-level and deep-sea temperature  
1311 variations over the past 40 million years. *Reviews of Geophysics* **60**, e2022RG000775  
1312 (2022).
- 1313 6. R. M. Spratt, L. E. Lisiecki, A Late Pleistocene sea level stack. *Climate of the Past* **12**,  
1314 1079-1092 (2016).
- 1315 7. J. Hansen, M. Sato, G. Russell, P. Kharecha, Climate sensitivity, sea level and atmospheric  
1316 carbon dioxide. *Philosophical Transactions of the Royal Society A-Mathematical Physical*  
1317 *and Engineering Sciences* **371**, 10.1098/rsta.2012.0294 (2013).
- 1318 8. J. E. Hansen *et al.*, Global warming in the pipeline. *Oxford Open Climate Change* **3**,  
1319 kgad008 (2023).
- 1320 9. P. U. Clark *et al.*, Mean ocean temperature change and decomposition of the benthic  $d^{18}\text{O}$   
1321 record over the last 4.5 Myr. *Climate of the Past*, (in review).
- 1322 10. J. D. Shakun, D. W. Lea, L. E. Lisiecki, M. E. Raymo, An 800-kyr record of global surface  
1323 ocean delta O-18 and implications for ice volume-temperature coupling. *Earth and*  
1324 *Planetary Science Letters* **426**, 58-68 (2015).
- 1325 11. S. Sosdian, Y. Rosenthal, Deep-sea temperature and ice volume changes across the  
1326 Pliocene-Pleistocene climate transitions. *Science* **325**, 306-310 (2009).
- 1327 12. H. Elderfield *et al.*, Evolution of ocean temperature and ice volume through the mid-  
1328 Pleistocene climate transition. *Science* **337**, 704-709 (2012).
- 1329 13. S. C. Woodard *et al.*, Antarctic role in Northern Hemisphere glaciation. *Science* **346**, 847-  
1330 851 (2014).
- 1331 14. H. L. Ford, M. E. Raymo, Regional and global signals in seawater  $\delta^{18}\text{O}$  records across the  
1332 mid-Pleistocene transition. *Geology* **48**, 113-117 (2020).
- 1333 15. K. G. Miller *et al.*, Cenozoic sea-level and cryospheric evolution from deep-sea  
1334 geochemical and continental margin records. *Science Advances* **6**, (2020).
- 1335 16. M. J. Winnick, J. K. Caves, Oxygen isotope mass-balance constraints on Pliocene sea level  
1336 and East Antarctic Ice Sheet stability. *Geology* **43**, 879-882 (2015).
- 1337 17. G. S. Dwyer, M. A. Chandler, Mid-Pliocene sea level and continental ice volume based on  
1338 coupled benthic Mg/Ca palaeotemperatures and oxygen isotopes. *Philosophical*  
1339 *Transactions of the Royal Society A-Mathematical Physical and Engineering Sciences* **367**,  
1340 157-168 (2009).
- 1341 18. K. A. Jakob *et al.*, A new sea-level record for the Neogene/Quaternary boundary reveals  
1342 transition to a more stable East Antarctic Ice Sheet. *Proceedings of the National Academy*  
1343 *of Sciences of the United States of America* **117**, 30980-30987 (2020).

1344 19. A. C. Mix, W. F. Ruddiman, Oxygen-isotope analyses and Pleistocene ice volumes.  
1345 *Quaternary Research* **21**, 1-20 (1984).

1346 20. G. R. Grant *et al.*, Reduced magnitude of Early Pleistocene intensification of Northern  
1347 Hemisphere Glaciation. *Quaternary Science Reviews* **349**, (2025).

1348 21. G. R. Grant *et al.*, The amplitude and origin of sea-level variability during the Pliocene  
1349 epoch. *Nature* **574**, 237-241 (2019).

1350 22. E. Gasson, R. M. DeConto, D. Pollard, Modeling the oxygen isotope composition of the  
1351 Antarctic ice sheet and its significance to Pliocene sea level. *Geology* **44**, 827-830 (2016).

1352 23. D. P. Schrag *et al.*, The oxygen isotopic composition of seawater during the Last Glacial  
1353 Maximum. *Quaternary Science Reviews* **21**, 331-342 (2002).

1354 24. K. Lambeck, H. Rouby, A. Purcell, Y. Sun, M. Sambridge, Sea level and global ice  
1355 volumes from the Last Glacial Maximum to the Holocene. *Proceedings of the National  
1356 Academy of Sciences* **111**, 15296-15303 (2014).

1357 25. N. Lhomme, G. K. C. Clarke, C. Ritz, Global budget of water isotopes inferred from polar  
1358 ice sheets. *Geophysical Research Letters* **32**, (2005).

1359 26. A. Sima, A. Paul, M. Schulz, J. Oerlemans, Modeling the oxygen-isotopic composition of  
1360 the North American Ice Sheet and its effect on the isotopic composition of the ocean during  
1361 the last glacial cycle. *Geophysical Research Letters* **33**, (2006).

1362 27. T. Tharammal, A. Paul, U. Merkel, D. Noone, Influence of Last Glacial Maximum  
1363 boundary conditions on the global water isotope distribution in an atmospheric general  
1364 circulation model. *Climate of the Past* **9**, 789-809 (2013).

1365 28. P. U. Clark, J. D. Shakun, Y. Rosenthal, P. Köhler, P. J. Bartlein, Global and regional  
1366 temperature change over the last 4.5 million years. *Science* **383**, 884-890 (2024).

1367 29. R. M. DeConto, D. Pollard, Contribution of Antarctica to past and future sea-level rise.  
1368 *Nature* **531**, 591-597 (2016).

1369 30. W. R. Peltier, D. F. Argus, R. Drummond, Space geodesy constrains ice age terminal  
1370 deglaciation: The global ICE-6G\_C (VM5a) model. *Journal of Geophysical Research-Solid  
1371 Earth* **120**, 450-487 (2015).

1372 31. M. B. Priestley, Evolutionary spectra and non-stationary processes. *Journal of the Royal  
1373 Statistical Society, Series B* **27**, 204-237 (1965).

1374 32. S. R. Meyers. (<https://cran.r-project.org/package=astrochron>, 2014).

1375 33. R. C. Team, in *R Foundation for Statistical Computing*. (Vienna, Austria, 2022).

1376 34. D. J. Thomson, Spectrum estimation and harmonic analysis. *Proceedings of the IEEE* **70**,  
1377 1055-1096 (1982).

1378 35. S. Developers. (2013).

1379 36. P. Howell, N. Pisias, J. Ballance, J. Baughman, L. Ochs, ARAND Time-Series Analysis  
1380 Software. (2006).

1381 37. D. Pollard, S. L. Thompson, Climate and ice-sheet mass balance at the Last Glacial  
1382 Maximum from GENESIS version 2 global climate model. *Quaternary Science Reviews*  
1383 **16**, 841-863 (1997).

1384 38. S. L. Thompson, D. Pollard, Greenland and Antarctic mass balances for present and  
1385 doubled atmospheric CO<sub>2</sub> from the GENESIS version-2 global climate model. *Journal of  
1386 Climate* **10**, 871-900 (1997).

1387 39. I. Janssens, P. Huybrechts, The Treatment of Meltwater Retardation in Mass-Balance  
1388 Parameterizations of the Greenland Ice Sheet. *Annals of Glaciology* **31**, 133-140 (2000).

1389 40. J. Laskar *et al.*, A long term numerical solution for the insolation quantities of the Earth.  
1390 *Astronomy and Astrophysics* **428**, 261-285 (2004).

1391 41. B. Honisch, N. G. Hemming, D. Archer, M. Siddall, J. F. McManus, Atmospheric Carbon  
1392 Dioxide Concentration Across the Mid-Pleistocene Transition. *Science* **324**, 1551-1554  
1393 (2009).

1394 42. K. A. Dyez, B. Honisch, G. A. Schmidt, Early Pleistocene Obliquity-Scale pCO(2)  
1395 Variability at similar to 1.5 Million Years Ago. *Paleoceanography and Paleoclimatology*  
1396 **33**, 1270-1291 (2018).

1397 43. G. Bartoli, B. Honisch, R. E. Zeebe, Atmospheric CO<sub>2</sub> decline during the Pliocene  
1398 intensification of Northern Hemisphere glaciations. *Paleoceanography* **26**, (2011).

1399 44. L. Tarasov, A. S. Dyke, R. M. Neal, W. R. Peltier, A data-calibrated distribution of  
1400 deglacial chronologies for the North American ice complex from glaciological modeling.  
1401 *Earth and Planetary Science Letters* **315**, 30-40 (2012).

1402 45. P. U. Clark, D. Pollard, Origin of the middle Pleistocene transition by ice sheet erosion of  
1403 regolith. *Paleoceanography* **13**, 1-9 (1998).

1404 46. S. Ahn, D. Khider, L. E. Lisiecki, C. E. Lawrence, A probabilistic Pliocene–Pleistocene  
1405 stack of benthic  $\delta^{18}\text{O}$  using a profile hidden Markov model. *Dynamics and Statistics of the*  
1406 *Climate System* **2**, 1-16 (2017).

1407 47. K. G. Miller *et al.*, High tide of the warm Pliocene: Implications of global sea level for  
1408 Antarctic deglaciation. *Geology* **40**, 407-410 (2012).

1409 48. O. A. Dumitru *et al.*, Constraints on global mean sea level during Pliocene warmth. *Nature*  
1410 **574**, 233-236 (2019).

1411 49. F. D. Richards *et al.*, Geodynamically corrected Pliocene shoreline elevations in Australia  
1412 consistent with midrange projections of Antarctic ice loss. *Science Advances* **9**, (2023).

1413 50. O. A. Dumitru *et al.*, Sea-level stands from the Western Mediterranean over the past 6.5  
1414 million years. *Sci Rep-Uk* **11**, 6681 (2021).

1415 51. A. Dutton, J. M. Webster, D. Zwart, K. Lambeck, B. Wohlfarth, Tropical tales of polar  
1416 ice: evidence of Last Interglacial polar ice sheet retreat recorded by fossil reefs of the  
1417 granitic Seychelles islands. *Quaternary Science Reviews* **107**, 182-196 (2015).

1418 52. K. M. Grant *et al.*, Sea-level variability over five glacial cycles. *Nature Communications*  
1419 **5**, (2014).

1420 53. Y. Yokoyama *et al.*, Rapid glaciation and a two-step sea level plunge into the Last Glacial  
1421 Maximum. *Nature* **559**, 603-+ (2018).

1422

1423